Retrieval Algorithm for Aerosol Effective Height from the Geostationary Environment Monitoring Spectrometer (GEMS)

Sang Seo Park[1,*], Jhoon Kim[2], Yeseul Cho[2], Hanlim Lee[3], Junsung Park[3], Dong-Won Lee[4], Won-Jin Lee[4], Deok-Rae Kim[4]

[1] *Department of Urban and Environmental Engineering, Ulsan National Institute of Science and Technology, Ulsan, Korea*

[2]*Department of Atmospheric Sciences, Yonsei University, Seoul, Korea*

[3]*Division of Earth and Environmental System Sciences, Pukyong National University, Busan, South Korea*

[4]*Envionment Satellite Center, National Institute of Environmental Research, Incheon, Korea*

[*]Corresponding author. Sang Seo Park (sangseopark@unist.ac.kr)

Submitted to Atmospheric Measurement Techniques

2023. 06.

Abstract

An algorithm for aerosol effective height (AEH) was developed for operational use with observations from the Geostationary Environment Monitoring Spectrometer (GEMS). The retrieval technique uses the slant column density of the oxygen dimer (O_2-O_2) at 477 nm, which is converted into AEH after retrieval of aerosol and surface optical properties from GEMS operational algorithms. The retrieved AEHs provide continuous vertical information of severe dust plumes over East Asia with reasonably good validation results and the collection of plume height information for anthropogenic aerosol pollutants over India. Compared to the AEH retrieved from Cloud-Aerosol Lidar with Orthogonal Polarization (CALIOP), the retrieval results show bias of -0.03 km with a standard deviation of 1.4 km for the AEH difference over the GEMS observation domain from January to June, 2021. The AEH difference depends on aerosol optical properties and surface reflectance. Compared to the aerosol layer height obtained from the tropospheric monitoring instrument (TROPOMI), differences of 1.50 ± 1.08 km, 1.59 ± 1.22 km, and 1.71 ± 1.24 km were obtained for pixels with single scattering albedo (SSA) < 0.90, 0.90 < SSA < 0.95, and SSA > 0.95, respectively.

Keywords: aerosol effective height, aerosol optical depth, environmental satellite, GEMS

1. Introduction

Since the launch of the Total Ozone Mapping Spectrometer (TOMS) on Nimbus-7, ultraviolet (UV)-visible satellite measurements have been used for environmental monitoring of the distribution and reaction processes of pollutants (e.g., anthropogenic aerosols, tropospheric ozone, NO_2, and SO_2). Measurements from environmental satellites have been used to estimate gaseous species in the atmosphere, resulting in vertical column integrated amounts. However, these column-integrated amounts and associated surface concentrations have uncertainty due to simultaneous changes in optical path length associated with the vertical distribution of target species and amounts of scattering materials (clouds and aerosols) present. In addition, aerosol vertical information is also important information for the application of tropospheric concentration of aerosols. For example, aerosol height information in the free troposphere is particularly important for aviation safety by affecting the visibility. Also, scientific applications including radiative forcing studies, long-range transport modelling and studies of cloud formation processes have been used aerosol vertical information as an input parameter.

Environmental satellite sensors, that measure UV-visible wavelength, have been used the UV aerosol index (UVAI) for aerosol detection (e.g., Buchard *et al.*, 2015; Herman *et al.*, 1997; Torres *et al.*, 1998, 2002; Prospero *et al.*, 2000; de Graaf *et al.*, 2005). Furthermore, scattering radiative index values were investigated for the possibility of the cloud signal detection (Penning de Vries *et al.*, 2009, 2015; Kooreman *et al.*, 2020; Kim *et al.*, 2018). However, these indices only have qualitative characteristics and limitations to identify aerosol amounts.

For the quantitative estimation, measurements of aerosol optical depth (AOD) and

67 radiative cloud fraction have also been retrieved from pixel-based radiance data in UV-
68 visible wavelength range. Recently, various aerosol retrieval algorithms have been
69 developed to be applied in passive satellite sensors. These algorithms focus on
70 improved trace gas retrieval as well as direct monitoring of aerosol properties, such as
71 AOD and single scattering albedo (SSA) (e.g., Ahn *et al.*, 2014; Kim *et al.*, 2020; Torres
72 et al., 2020).

73 Although the algorithms developed for environmental satellite sensors indicate the
74 presence and amounts of scattering materials, the accuracy of these retrieval algorithms
75 for trace gases is affected by the relative vertical distributions between trace gases and
76 scattering materials (e.g., Lorente *et al.*, 2017; Hong *et al.*, 2017). For this reason,
77 estimating cloud vertical parameters is important. For cloud vertical information, cloud
78 height information has been estimated simultaneously with cloud optical depth and
79 radiative cloud fraction data using the rotational Raman scattering (Joiner and Vasilkov,
80 2006; Vasilkov *et al.*, 2008; Joiner and Bhartia, 1995) and absorption intensity of the
81 oxygen dimer (O_2-O_2) (Accarreta *et al.*, 2004; Vasilkov *et al.*, 2018; Choi *et al.*, 2021)
82 combined with normalized radiance.

83 Similarly, the aerosol vertical distribution can be estimated using the oxygen
84 absorption bands, such as the O_2-O_2 (Park *et al.*, 2016; Chimot *et al.*, 2017; Choi *et al.*,
85 2019, 2020), O_2-A (Dubisson *et al.*, 2009; Geddes and Boesch, 2015; Sanders *et al.*,
86 2015; Xu *et al.*, 2017; Zeng *et al.*, 2020), and O_2-B (Chen *et al.*, 2021; Ding *et al.*,
87 2016) bands, as well as combinations of these bands (Sanghavi *et al.*, 2012; Chen *et al.*,
88 2021). In addition, an algorithm for aerosol vertical information has been developed
89 based on hyperspectral UV-visible radiance from satellite observation. Nanda *et al.*
90 (2018) demonstrated the possibility of aerosol height retrieval from the O_2-A band

91 developed an algorithm using Tropospheric Monitoring Instrument (TROPOMI)
92 (Sanders and de Haan, 2016; Nanda *et al.*, 2020) and implemented the algorithm
93 operationally.

94 However, the vertical distribution of aerosol is difficult to assess because of its large
95 spatio-temporal variability. Although the Cloud-Aerosol Lidar with Orthogonal
96 Polarization (CALIOP) provided the aerosol vertical distribution with high vertical
97 resolution (Omar et al., 2009), other passive satellite sensors are only able to estimate
98 the representative parameter of aerosol height. Veihelmann et al. (2007) showed that the
99 number of degrees of freedom of signal for aerosol is 2-4 for most satellite observation
100 conditions by the ozone monitoring instrument (OMI). In addition, the number of
101 degrees of freedom is not exceeded to 3 from the shortwave satellite measurements (e.g.,
102 Rao et al., 2019; Choi et al., 2021). It means that the amount of information for aerosol
103 vertical distribution has a limitation for satellite sensor. Because of limitation for
104 describing the aerosol vertical information, aerosol layer height (ALH) (e.g., Nanda et
105 al., 2018) or aerosol effective height (AEH) (Park et al., 2016) were defined to retrieve
106 the aerosol vertical information from the passive satellite sensors.

107 The Geostationary Environment Monitoring Spectrometer (GEMS), which was
108 launched by South Korea in February 2020, provides column density of ozone, aerosol,
109 and their precursors (Kim *et al.*, 2020). The main purpose of GEMS is to monitor air
110 quality, and aerosol properties are targets of such monitoring over East Asia. For this
111 reason, the GEMS aerosol algorithm was developed as multiple operational products.
112 The Aerosol algorithm adopted optimal estimation method (Rogers, 2000) to retrieve
113 AOD, SSA, and aerosol layer height (ALH). Aerosol properties are obtained for the
114 purposes of monitoring air quality and aerosol effects for the air mass factor (AMF)

115 calculation. In addition to these aerosol products, AEH is provided to represent upper
116 layer of the peak. Both ALH and AEH help understand the vertical structure of aerosol
117 layer. For the possibility for development of an AEH retrieval algorithm, Park *et al.*
118 (2016) conducted theoretical sensitivity testing of AEH retrieval using solely the O_2-O_2
119 absorption band along with aerosol and surface properties. Overall, the sensitivity of
120 AEH retrieval was strongly affected by SSA, AOD, and aerosol types including optical
121 and size properties. In addition, case studies of AEH during dust transport over East
122 Asia were conducted using radiance data from the Ozone Monitoring Instrument (OMI)
123 and aerosol optical properties from the Moderate Resolution Imaging Spectroradiometer
124 (MODIS).

125 Based on theoretical considerations and case study results, we introduce an
126 operational retrieval algorithm for AEH. Section 2 introduces the details of satellite
127 sensors for the comparison and colocation method in this study. Section 3 describes the
128 details of the AEH retrieval algorithm for GEMS and provides a list of the detailed input
129 parameters. Section 4 reports retrieval results based on case studies of aerosol transport,
130 and section 5 contains long-term validation results based on CALIOP and TROPOMI
131 data. Finally, in section 6, the summary and main conclusions are presented.

132

133 **2. Data**

134 **2.1 GEMS**

135 The GEMS instrument on board the Geostationary Korea multipurpose satellite 2B
136 (GK2B) is located at 128.2°E, and scans from 145°E to 75°E with north-south coverage
137 of 5°S-45°N. The GK2B observation schedule shares the GEMS and the Geostationary
138 Ocean Color Imager 2 (GOCI2), and the GEMS scan the 30 minutes duration from

every hour from 45 minutes to 15 minutes during daytime. The spatial resolution of GEMS is 3.5 km (North-South) × 8 km (East-West) for aerosol and gaseous products at 38°N. The spectral range of 300-500 nm is covered with a spectral resolution (as defined by the full-width and half-maximum of the spectral response function) of 0.6 nm and a spectral sampling of 0.2 nm.

The GEMS Level 2 aerosol operational algorithm (L2AERAOD) retrieves the aerosol index (AI) values for UV and visible wavelengths, as well as AOD and SSA after determining the aerosol types (National Institute of Environmental Research, 2020). The aerosol types are defined as absorbing, non-absorbing, and dust types by using the AI based classification methods exploiting measurements in the UV and visible (e.g., Go et al., 2020). Park *et al.* (2016) noted that the error budget of AEH is significantly affected by uncertainty in AOD and SSA and by the misclassification of aerosol types, which is directly related to the optical property and size information. Overall, uncertainties of 0.2 in AOD, of 20% in particle size, of 10% in SSA, and 0.02 in surface albedo cause AEH errors in the range 739-1276 m (Park et al., 2016). In this study, the L2AERAOD results for AOD at 550 nm and SSA at 443 nm were adopted as input data for aerosol properties, and the AOD and SSA values were spectrally converted to those values at assumed wavelength for the inversion calculation process after considering the spectral dependence of the aerosol optical properties by the aerosol models. In addition, we also used the minimum reflectance under the Lambertian assumption to retrieve AOD and AEH to coincide with the use of surface information on L2AERAOD and AEH retrieval.

2.2. TROPOMI

TROPOMI is a nadir-viewing spectrometer, the only payload of the Sentinel-5

Precursor (S5P), measuring radiance in the UV, visible, near-infrared, and the shortwave IR (Veefkind et al., 2012). The S5P is a polar orbit satellite that crosses the equator at 13:30 local time at an ascending node. The aerosol layer height product from TROPOMI (AER_LH) provides vertically localized aerosol layers in the free troposphere with cloud free condition by using the level 1b earth radiance measurements from 758 to 770 nm (de Graaf *et al.*, 2022). The definition of ALH from TROPOMI is the optical centroid layer height of the plume above sea level. The spectral fit employs a fast forward model based on a neural network for simulated condition of reflectance around the O_2-A band. After cloud masking, an optimal estimation method is used to retrieve the ALH and AOD by the inversion method from observation. Other aerosol parameters, such as SSA, layer thickness, and scattering phase function, are assumed to be fixed values (Nanda et al., 2020). Furthermore, the ALH retrieval has limitation to the aerosol plume with higher than 12 km, because the ALH neural network product currently provides the plume pressure range of 75-1000 hPa (Michailidis et al., 2023).

The main purpose of the AER_LH product is the retrieval of aerosol layers in the free troposphere (desert dust, biomass burning, and volcanic ash) (Michailidis et al., 2023). The target requirement on the accuracy and precision is 0.5 km or 50 hPa, and the threshold requirement is 1 km or 100 hPa under the elevated aerosol plumes with cloud-free conditions for the layer height and for the associated pressure, respectively (de Graaf et al., 2022, Veefkind et al., 2012). However, the TROPOMI ALH product has strong dependence of the surface albedo, especial to the bright surfaces (Sanders et al., 2015). From Michailidis et al. (2023), a mean bias of -0.51±0.77 and -2.27±1.17 km is estimated over ocean and land, respectively. In this study, we use version 02.04.00 of

187 the TROPOMI offline level 2 AER_LH product (European Space Agency, 2021) with
188 the spatial resolution is 3.5 km × 5.5 km at nadir viewing geometry.
189
190 **2.3. CALIOP**
191 The Cloud-Aerosol Lidar with Orthogonal Polarization (CALIOP) is a spaceborne
192 lidar onboard the Cloud-Aerosol Lidar and Infrared Pathfinder Satellite Observations
193 (CALIPSO) to measure the vertical information of aerosol and cloud with estimating
194 the optical properties. The CALIOP has two different wavelength channels (532 and
195 1064 nm) by using the Nd:YAG laser to generate the signals (Winker et al., 2009). The
196 CALIPSO is Sun synchronous orbit constellated to the A-train with period of 98.3
197 minutes. It crosses the equator at 13:30 local time on an ascending node. To cover the
198 GEMS observation area, we used CALIOP data of 3-4 orbits per day. For the vertical
199 information, the resolution for vertical sampling is 30 m below 8 km altitude, and 60 m
200 from 8 to 20 km altitude, respectively. Although the CALIOP retrieves the data with
201 extremely high horizontal and vertical resolutions, the spatial coverage is narrow
202 because the footprint of the CALIOP is about 90 m at the Earth surface. In this study,
203 the data of Level 2 aerosol profile product (APro, version 3.41) was used (Tackett et al.,
204 2018). The aerosol profile product simultaneously includes both aerosol and cloud
205 optical depth. In addition, extinction quality flag (Extinction_QC_Flag) data shows the
206 quality of extinction profile. In this study, we checked and used the quality flag value at
207 532 nm for the aerosol extinction coefficient profile data. The AOD from CALIOP is
208 vertically integrated aerosol extinction coefficient from surface to top of atmosphere,
209 and representative layer height parameters (ALH and AEH) are directly estimated by
210 using the vertical profile of aerosol extinction coefficient at 532 nm to minimize the

211 spectral discrepancy of aerosol extinction. For the ALH retrieval, we adopted mean
212 extinction height from the CALIOP extinction coefficient profile (e.g., Koffi et al.,
213 2012; Xu et al., 2019). Similarly, the AEH estimation from CALIOP is also used to the
214 extinction coefficient profile.
215
216 **2.4 Data Selection and Colocation**
217 In this study, we used data within 75°E-145°E for east-west and 5°S-45°N for north-
218 south direction, which is the observation area of GEMS. From Park et al. (2020), the
219 spatial range of highly coincident AOD is 30-40 km. To ensure that the number of
220 retrieved observation pixels that can be analyzed in this study is sufficiently high, we
221 relax the spatial limits for collocation matching. For spatial colocation, we selected
222 pixels for which distance between GEMS and CALIOP (or TROPOMI) observations
223 was less than 50 km. In addition, only the closest 10% of pixels were used. Given the
224 different orbital characteristics of CALIOP (or TROPOMI) and GEMS, temporal
225 colocation was also considered. During the period of image scanning from east to west
226 over Asia by GEMS, CALIOP and TROPOMI pass through the GEMS observation area
227 from south to north every 98.3 minutes. On average, two low earth orbit (LEO)
228 satellites pass three to four orbits through the GEMS scan area during a single day of
229 daytime observation. To consider these different orbital characteristics, only
230 observations taken within ±1 hour of the GEMS observation time was selected for
231 temporal colocation. As GEMS observes hourly, collocated pixels between the two
232 satellites shift from east to west over time.
233 To ensure the accuracy of ALH from TROPOMI, only pixels with quality assurance
234 (QA) values of 1.0 were used. To minimize the cloud contamination, the TROPOMI

ALH product uses the VIIRS cloud mask information and cloud parameters from the Fast Retrieval Scheme for Clouds from the Oxygen A-band (FRESCO). To consider the cloud contamination for the aerosol products, in addition, the VIIRS cirrus cloud reflectance (viirs_cirrus_reflectance < 0.4), VIIRS cloud mask (viirs_cloud_mask < 0.1), and cloud fraction from the FRESCO (cloud_fraction < 0.1) are considered in this study (Michailidis et al., 2023). However, de Graaf *et al.* (2022) showed that respective cloud masking methods have difficulty detecting various clouds. For this reason, cloud contamination remains a critical source of uncertainty in the ALH retrieval. From the previous studies, the UVAI is used to detect the presence of absorbing aerosol (e.g., Chen et al., 2021; Griffin et al., 2020; Michailidis et al., 2023; Sanders et al., 2015), and the aerosol height information was only retrieved on the absorbing aerosol pixels. However, the GEMS aerosol product is retrieved not only the absorbing aerosols, but also the non-absorbing aerosols. For this reason, the pixels for which with an AOD at 443 nm (AOD_{443} hereafter) taken from the GEMS aerosol product exceed 0.3 are selected for AEH retrieval.

3. AEH retrieval algorithm

AEH is a layer height parameter that considers the penetration of photons into the aerosol layer. It is defined such that the integral of the vertical aerosol extinction profile from the surface to the AEH is equal to $(1\text{-}e^{-1}) \times$ AOD, as defined by Park *et al.* (2016). Numerous previous studies have used the aerosol top layer height (Kohkanovsky and Rozanov, 2010) or middle layer height (i.e. ALH or centroid height) (e.g., Sanders *et al.*, 2015; Nanda *et al.*, 2020) as the aerosol vertical layer parameter. AEH is similar to the aerosol top layer height but with a slight bias.

For AEH retrieval, the vertical distribution assumption is also important. The Gaussian Density Fitting (GDF) distribution, which is a modified Gaussian distribution structure by considering the range of upper and lower boundary height, is assumed for AEH retrieval. The full-width at half-maximum (FWHM) of the aerosol layer is assumed to be 1 km. A schematic description of AEH and other aerosol vertical parameters are shown in Figure 1. Based on the assumptions about the aerosol vertical distribution, the AEH value is higher than the peak height of the Gaussian distribution and lower than the aerosol top layer height. Otherwise, the ALH is defined as the integral of the vertical aerosol extinction profile from the surface to the ALH is equal to 0.5 × AOD. This assumption is used by Nanda et al. (2016). Therefore, the ALH equals the peak height of the profile in the conditions shown in Figure 1.

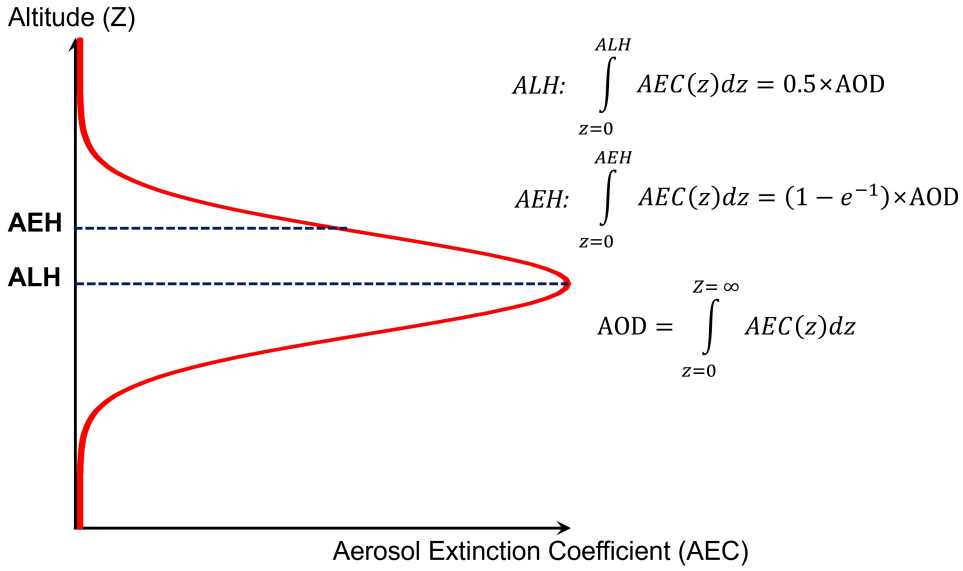

Figure 1. A schematic illustration of AEH and ALH definitions in an idealized Gaussian shape of aerosol vertical distribution.

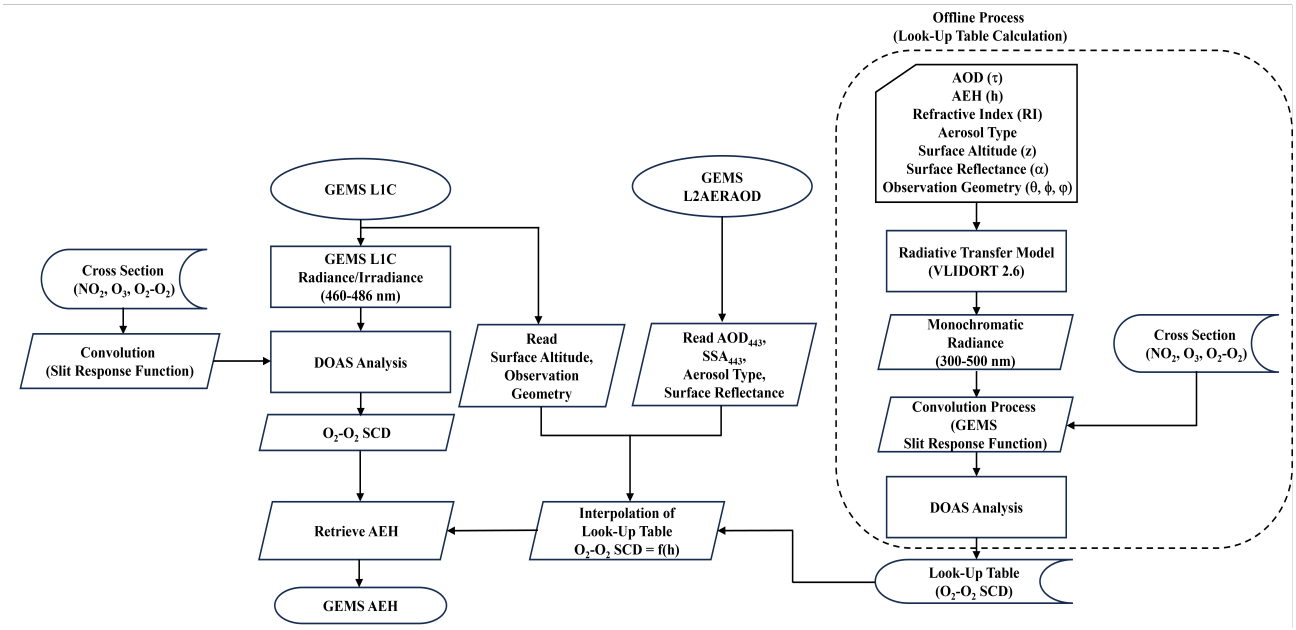

Figure 2. Flowchart of the AEH retrieval algorithm for GEMS satellite observation.

For AEH retrieval, the basic idea is the identification of changes in optical path length caused by effective aerosol layer height variation. To measure the optical path length change, O_2-O_2 SCD retrieved by the DOAS method was used because the spectral coverage is limited to 300-500 nm (Park et al., 2016, Kim et al., 2020). In the GEMS product, the O_2-O_2 SCD at 477 nm absorption band is the most useful absorption band because this absorption band is strongest absorption band within the GEMS spectral observation range. Figure 2 shows the overall flowchart of the AEH algorithm for GEMS satellite. The AEH algorithm for GEMS employs a look-up table (LUT) that contains O_2-O_2 slant column density (SCD) values for many scenarios with a variety of observation geometries [solar zenith angle (SZA; θ), viewing zenith angle (VZA; Φ), relative azimuth angle (RAA; φ)], surface altitude (z), surface albedo (α), AOD (τ), AEH (h), Refractive Index (RI) for SSA, and aerosol type. During the radiance simulation, the radiance is monochromatically simulated and then convolved with the

GEMS instrument spectral response function. Finally, the radiance information is converted to the O_2-O_2 SCD from differential optical absorption spectroscopy (DOAS) method (Platt, 1994).

DOAS method has been frequently used to estimate the amount of trace gases (i.e., SCD of trace gas) from ground (e.g., Cheng et al., 2023; Irie et al., 2008; Platt and Stutz, 2008; Wagner et al., 2011; Wang et al., 2017) and satellite (e.g., Kwon et al., 2019; Li et al., 2023; Wagner et al., 2007, 2010) measurements. Detailed DOAS fitting parameter and setting information is provided in Table 1 for the estimation of O_2-O_2 SCD from both the simulation and observation data. For the O_2-O_2 SCD estimation at 477 nm, the fitting window is ranged from 460 to 486 nm to cover the full absorption structure of O_2-O_2. Within the fitting window, the absorptions of NO_2 and O_3 are significant. To describe these two absorbing species, temperature dependent cross section information is adopted. The temperature dependent cross section setting considers stratosphere and troposphere, simultaneously.

Table 1. Details of fitting parameter for O_2-O_2 SCD estimation via the DOAS method.

Parameter	
Fitting window	460 – 486 nm
Absorption cross section	NO_2 at 220 and 294 K (Vandaele *et al.*, 1998) O_3 at 223, 243 and 293K (Bogumil *et al.*, 2001) O_2-O_2 at 293 K (Thalman and Volkamer, 2013) Ring

307 **Table 2.** Ratio between SCD error and the SCD of O_2-O_2 according to the polynomial
308 order and offset settings used for DOAS fitting.

Polynomial	Offset = none	Offset = 0^{th}
2^{nd} order	6.06 ± 2.07	6.79 ± 2.31
3^{rd} order	6.32 ± 2.20	6.79 ± 2.32
4^{th} order	7.86 ± 2.78	7.34 ± 2.85

309

310 To minimize the noise effect and improve DOAS fitting quality, the optimal settings
311 for fitting were also analyzed. Table 2 shows ratios of O_2-O_2 SCD error to the O_2-O_2
312 SCD for various polynomial and bias orders from observed radiance. The polynomial
313 and offset are basic fitting parameters for the DOAS fitting. Two parameters describe
314 the broadband spectral feature of radiance before identifying the gas absorption
315 structure. The ratio between SCD error and the SCD of O_2-O_2 is important to determine
316 the AEH retrieval quality. When the fitting error increases, the uncertainty of AEH is
317 also enhanced during the retrieval. Smallest AEH fitting errors are obtained by a DOAS
318 fit with a 2^{nd} order of polynomial, and 'none' offset. These settings are used in the
319 GEMS AEH algorithm.
320 In estimating AEH, other aerosol characteristics, including AOD and aerosol optical
321 properties, affect retrieval accuracy. Park et al. (2016) have shown that the largest
322 contributor to the AEH uncertainty is associated with the uncertainty in SSA. In
323 addition, the AEH retrieval uncertainty due to error in the aerosol optical properties (e.g.,
324 AOD and phase function) and surface albedo has dependence of observation geometries.
325 After the estimation of O_2-O_2 SCD, for this reason, conversion from O_2-O_2 SCD to

AEH is an essential process. Table 3 shows dimensions of the LUT for the AEH retrieval algorithm. To calculate the LUT, a linearized pseudo-spherical vector discrete ordinate radiative transfer model (VLIDORT) version 2.6 was used (Spurr, 2013). During the radiative transfer model simulation, reference wavelength for the SSA and AOD is assumed to be 440 nm. The aerosol type is defined by the radiative absorptivity and particle size information. The aerosol type is classified as absorbing, dust, and non-absorbing aerosol. Absorbing and non-absorbing aerosol types are assumed to the fine-mode dominant particles. For the spectral conversion of AOD, the angstrom exponent of 1.186, 0.222, and 1.179 are used for absorbing, dust, and non-absorbing aerosol, respectively. The SSA is assumed to be spectrally constant within the spectral range for O_2-O_2 estimation. Although the spectral O_2-O_2 absorption band is around 477 nm, the spectral discrepancy between reference wavelength for aerosol optical properties and center wavelength of O_2-O_2 absorption is assumed to be ignored in this study. After calculating spectral radiance with 0.1 nm sampling, the convolution with the GEMS slit response function was applied, and the spectra were sampled on the spectral grid of the GEMS radiance data (Level 1C) prior to the DOAS fitting. Radiative transfer calculations were performed accounting for the temperature dependence of absorption cross section for O_2-O_2 (e.g., Park *et al.*, 2017).

350 **Table 3.** The dimension of the LUT for the GEMS AEH retrieval algorithm used to
351 estimate AEH from O_2-O_2 SCD. (SZA: solar zenith angle, VZA: viewing zenith angle,
352 RAA: relative azimuth angle, SUR: surface reflectance).

Variable [unit]	**No. of entries**	**Entries**	
Spectral range [nm]	-	455-491 nm (0.1 nm interval)	
SZA [º]	7	0.01, 10, 20, 30, 40, 50, 60	
VZA [o]	7	0.01, 10, 20, 30, 40, 50, 60	
RAA [o]	10	0.01,20, 40, 60, 80, 100, 120, 140, 160, 180	
SUR	3	0.0, 0.05, 0.2	
AOD at 440 nm	11	0.04, 0.2, 0.4, 0.7, 1.0, 1.3, 1.6, 2.0, 2.5, 3.0, 5.0	
Refractive Index (Imaginary) at 440 nm	3×3	**Absorbing** (Real: 1.45)	0.000, 0.0074, 0.0314
		Dust (Real: 1.53)	0.0, 0.0030, 0.0080
		Non-Absorbing (Real: 1.41)	0.0, 0.0040, 0.0156
AEH [km]	13	0.0 (Extrapolate), 0.2, 0.5, 1.0, 1.3,1.6, 2.0, 2.3, 2.7, 3.0, 3.5, 5.0, 10.0 (Extrapolate)	
Terrain Height [km]	2	0.0, 2.0	

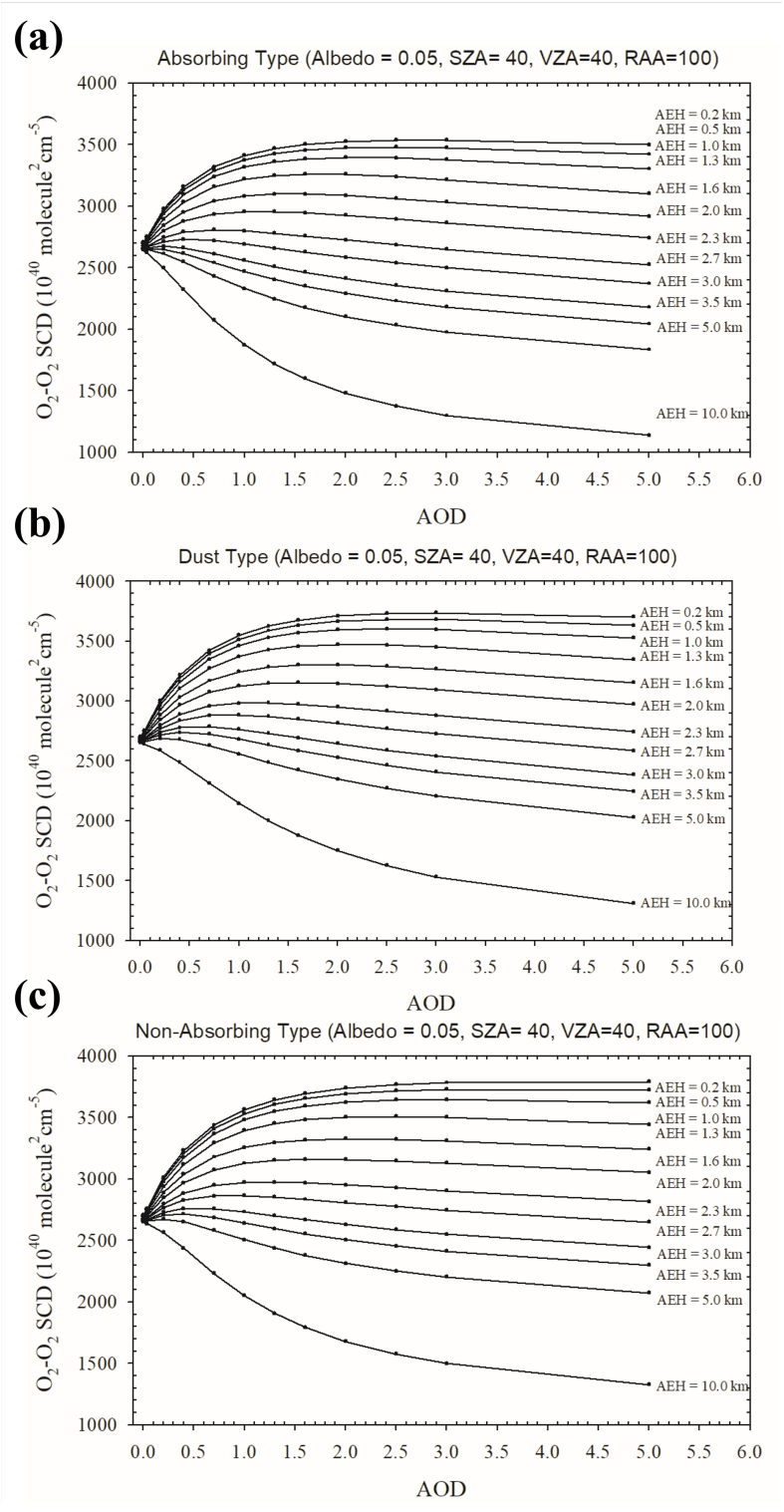

Figure 3. O_2-O_2 SCD dependence as a function of AOD and AEH for (a) Absorbing, (b) Dust, and (c) Non-Absorbing aerosol types.

Figure 3 shows the example of O_2-O_2 SCD dependence as a function of AOD and AEH from the LUT according to the respective aerosol types and AOD. O_2-O_2 SCD decreases with increasing AEH for all aerosol types and AOD (Park *et al.*, 2016). Similar to the previous study, the O_2-O_2 SCD sensitivity is enhanced at high AOD and absorbing aerosol cases from GEMS LUT. In addition, the contrast of O_2-O_2 SCD is greater for absorbing aerosols than non-absorbing aerosols. During the radiance passing through the aerosol layer, the absorbing aerosol is more efficiently absorbed the radiance. For this reason, the effective optical path length is significantly shorter for absorbing aerosols.

The AEH algorithm used the GEMS operational AOD and surface reflectance. However, those retrieval results include the uncertainties. Figure 4 shows the AEH retrieval uncertainty based on the O_2-O_2 SCD LUT with an AOD error of 0.2. The retrieval uncertainty of AEH was evaluated as the relative ratio of SCD changes with respect to input variables. This ratio is defined by the relationship between changes in SCD per unit AEH and changes in SCD due to uncertainties in input variables. The AOD error of 0.2 is twice the target accuracy of the GEMS standard algorithm product. Because the O_2-O_2 SCD change is small in high AOD, the AEH retrieval uncertainty is relatively small in high AOD condition. In addition, the SCD sensitivity in high AEH is weak due to the vertical distribution characteristics of O_2-O_2. Thus, the AEH uncertainty is up to 0.9 km at high AEH case in moderate AOD cases (around 0.5-1.0).

Figure 5 shows the AEH retrieval uncertainty with the surface reflectance error of 0.02. Because surface reflection and aerosol scattering simultaneously affect the increase in optical path length, surface reflectance uncertainty has a significant impact especially to low AOD. The AEH retrieval error due to uncertainty in surface

reflectance is larger than 1 km in cases with AOD < 0.4. In addition, the AEH error by the surface reflectance uncertainty linearly decreases with increasing AOD, indicating relatively small impact with aerosol height change.

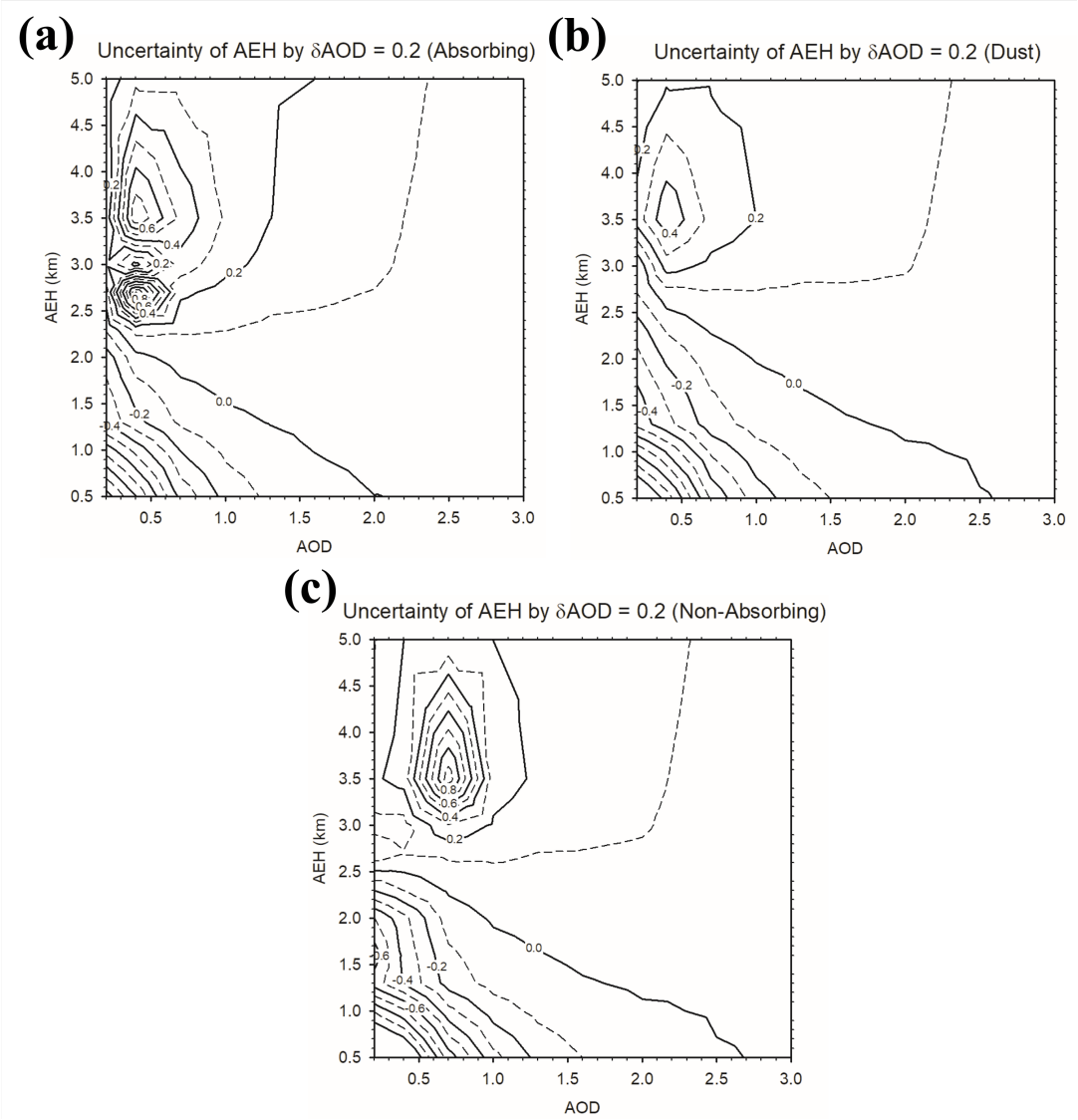

Figure 4. AEH retrieval uncertainty due to an the AOD error of 0.2 for cases with (a) Absorbing, (b) Dust, and (c) Non-Absorbing aerosol types.

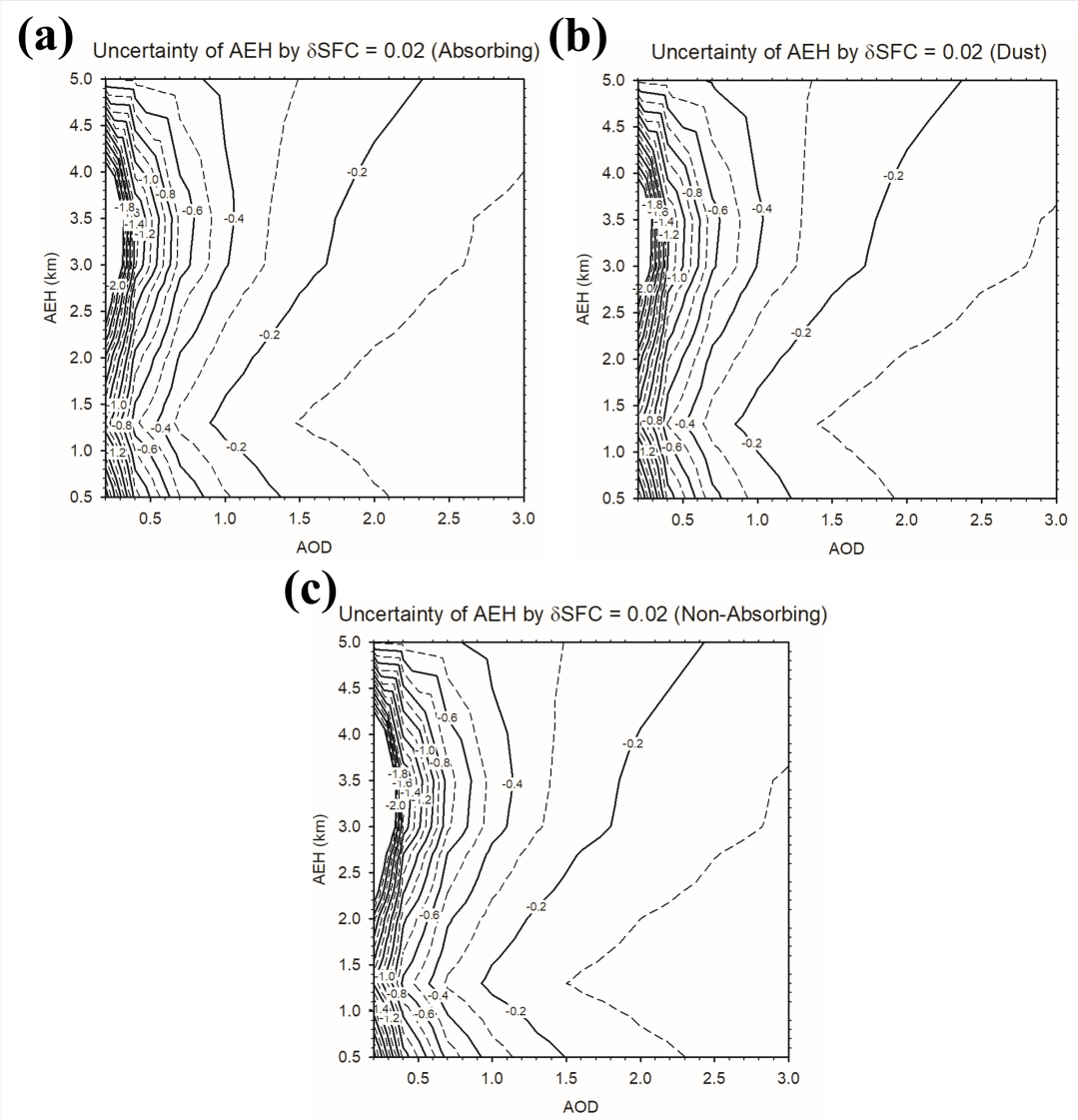

387

388 **Figure 5.** AEH retrieval uncertainty due to the surface reflectance error of 0.02 for

389 cases with (a) Absorbing, (b) Dust, and (c) Non-Absorbing aerosol types.

390

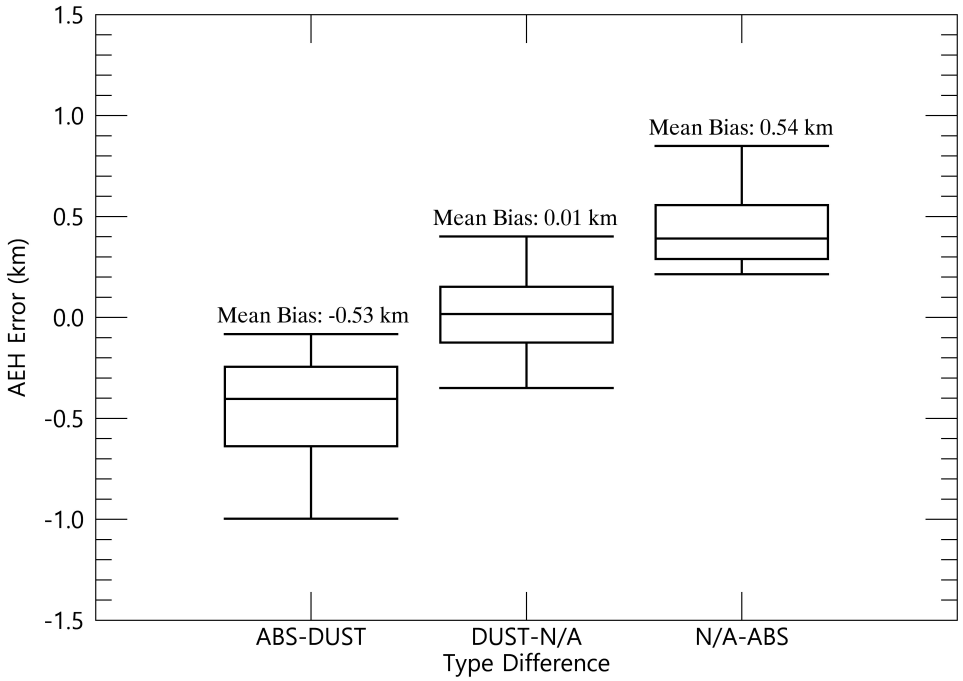

Figure 6. AEH retrieval uncertainty caused by the aerosol type misclassification.

Figure 6 shows the retrieval uncertainty caused by misclassification of the aerosol types. On average, the AEH retrieval uncertainty takes values up to 0.5 km, but this uncertainty shows larger than 2 km under low AOD and short optical path length conditions. From the sensitivity analysis, aerosol type (in terms of SSA) and AOD, and surface reflectance are carefully considered as input parameters for AEH retrieval.

In the AEH retrieval, the AOD, aerosol type, and SSA are obtained from the L2AERAOD, which is standard aerosol product of GEMS. The aerosol vertical distribution is always fixed as GDF function profiles as shown in Spurr and Christi (2014).

4. Case studies

Figure 7 shows retrieval results for AEH from GEMS on March 29 over East Asia. Because the operational schedule is hourly during the daytime, the GEMS retrieval results are shown at 1-hour intervals from 01:00 to 07:00 Universal Time Coordinated (UTC). AOD_{443} and SSA at 443 nm (SSA_{443} hereafter) are also shown in Figures S1 and S2, respectively. Pixels with low AOD_{443} values have large AEH uncertainty due to weak aerosol scattering information (see also Park *et al.*, 2016). For this reason, only AEH retrieval results with AOD greater than 0.3 are shown in this study. In addition, the AEH retrieval results are only shown to the "Reliable" quality flag of L2AERAOD, which is estimated to the aerosol optical properties with significant averaging kernel for optimal estimation in L2AERAOD. A case was analyzed in which a dust plume was located along the coast of China and South Korea with AOD_{443} of 0.8-1.2. Simultaneously, another plume was also present over the northeastern Korean Peninsula with AOD_{443} of 1.0-2.0. SSA_{443} was 0.90-0.93 for the plume over South Korea and 0.87-0.90 for the plume over the northeastern Korean Peninsula. Retrieved AEH results from these different plumes show similar ranges. For both detected plumes, the AEH shows similar patterns and takes values ranging between 1.0 and 2.0 km in this case.

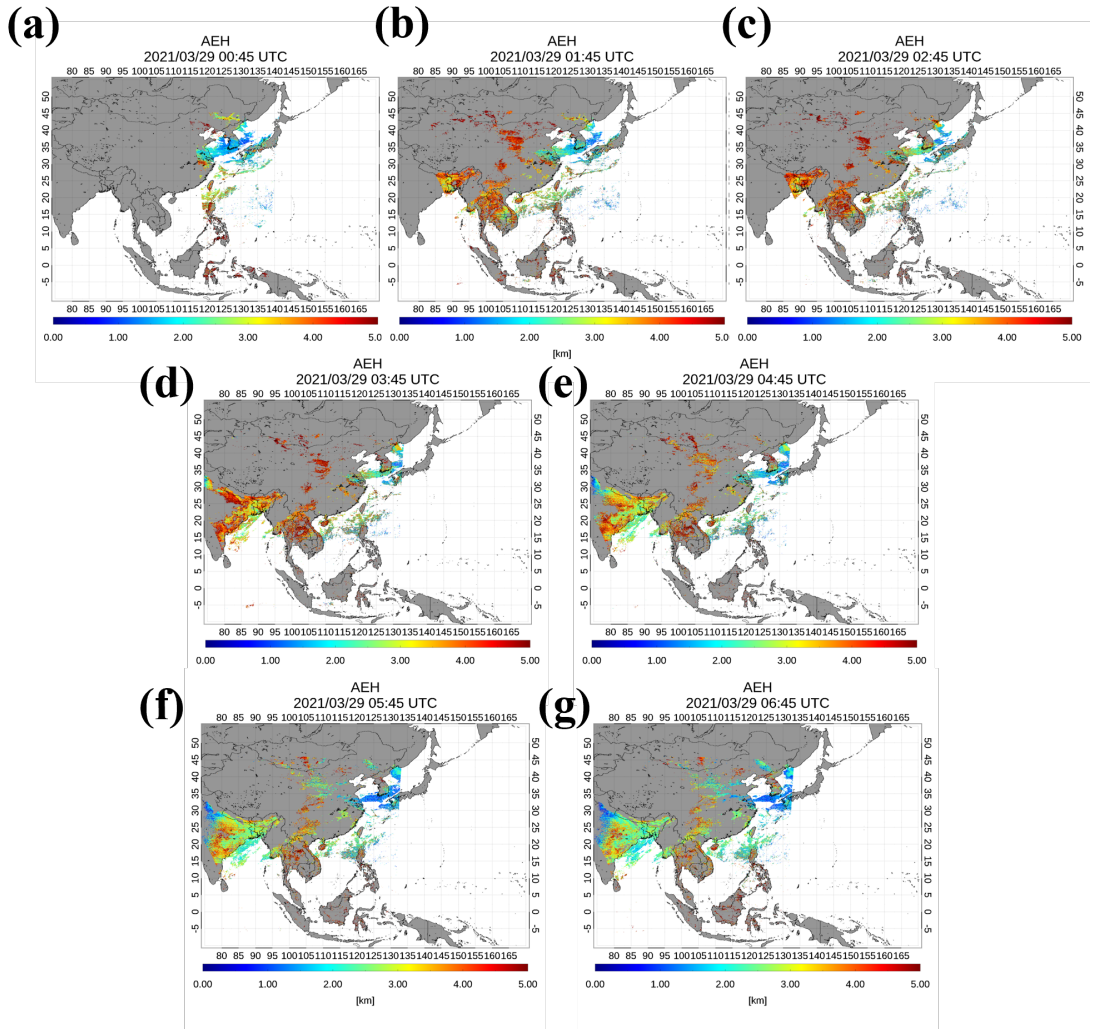

Figure 7. Case study results for AEH based on GEMS observations on March 29, 2021 [(a) 00:45 UTC, (b) 01:45 UTC, (c) 02:45 UTC, (d) 03:45 UTC, (e) 04:45 UTC, (f) 05:45 UTC, and (g) 06:45 UTC].

An additional severe aerosol plume was present over northeastern India, with AOD_{443} of 1.0-2.0 and SSA_{443} of 0.85-0.90. According to Rana *et al.* (2019), metropolitan cities and industrial clusters in India are heavy emitters of black carbon, and high concentrations of black carbon are distributed over the Indo-Gangetic Plain (IGP). Therefore, the aerosol plume with high AOD and low SSA (high absorbing) is

considered a physical rather than an artifact due to edge of GEMS observation field. Except for the inland parts of India, AEH in high AOD pixels ranged from 1.5 to 3.5 km.

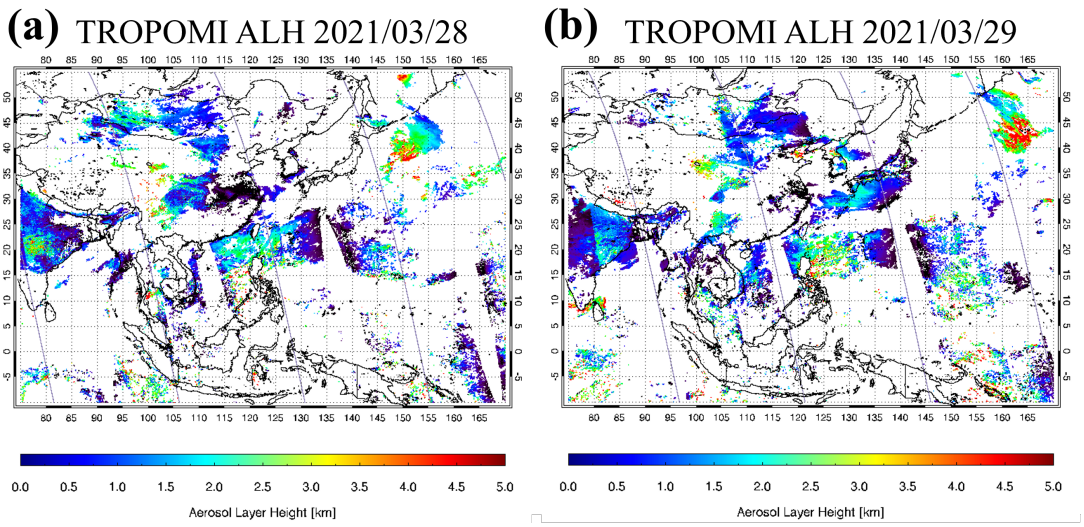

Figure 8. ALH retrieved from TROPOMI and orbit path of CALIOP on (a) March 28 and (b) March 29, 2021 (Unit: km).

For comparison of the retrieval, Figure 8 shows the ALH retrieved from TROPOMI on March 28 and 29, 2021 over East Asia. A dust plume was transported from China to South Korea during this period, then split into two distinct plumes over northeastern China and the coastal area of South Korea. The ALH retrieved from TROPOMI for both plumes range between 0.5 and 1.5 km. Given the difference in definition for the aerosol height parameters between ALH and AEH as shown in Fig. 1, AEH values retrieved from GEMS were higher than the ALH values retrieved from TROPOMI. In an ideal case under symmetric gaussian distribution with a width of 1 km, the AEH from GEMS was around 0.5 km higher than the peak height of aerosol layer. The ALH expresses the center (or peak) height, thus, the AEH from GEMS was overestimated by around 0.5 km relative to the ALH from TROPOMI. Although AEH had higher values than ALH from

TROPOMI, the GEMS AEH retrieval provided meaningful physical results for the dust transport case study.

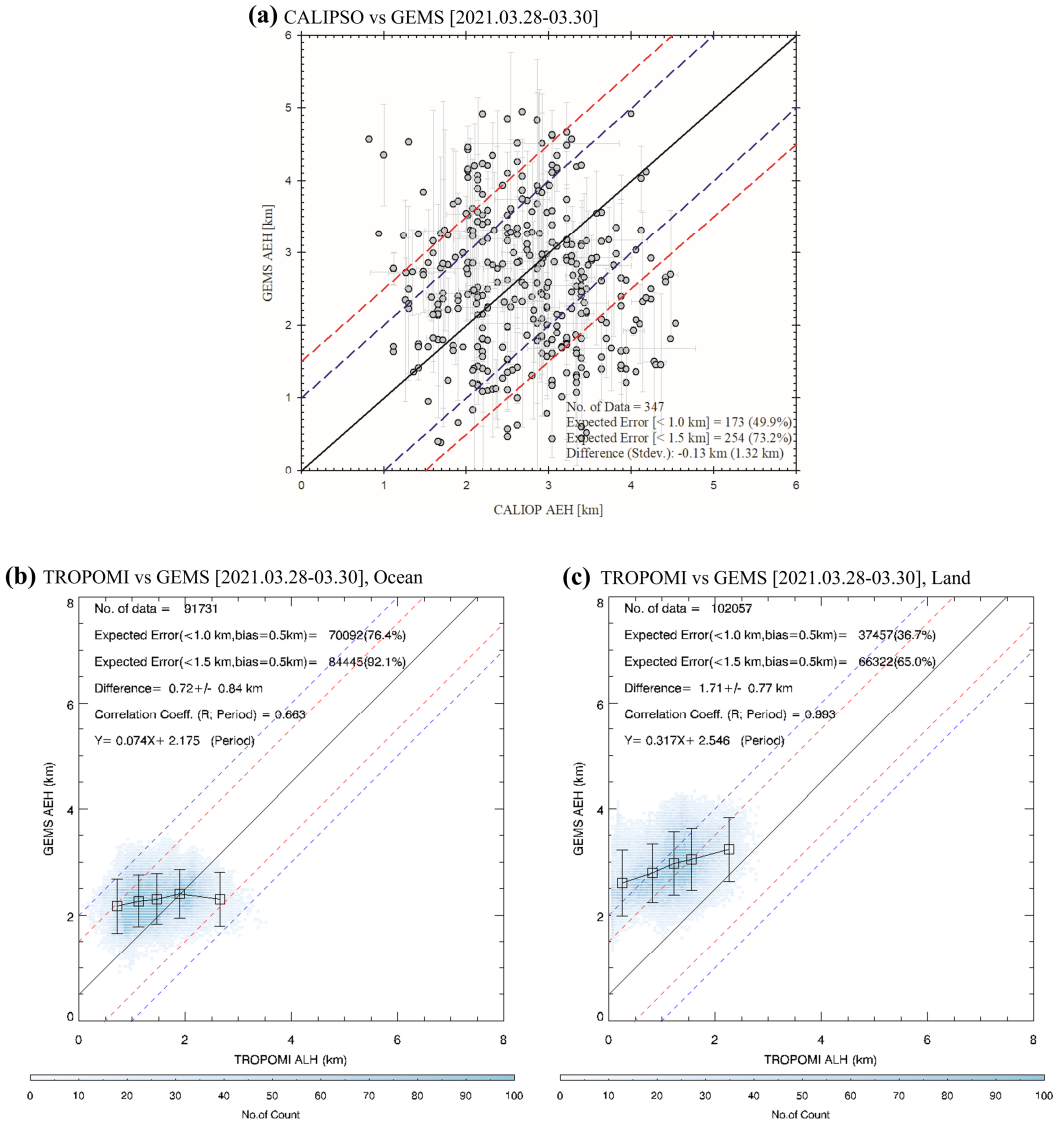

Figure 9. Intercomparison of (a) AEH between CALIOP and GEMS and (b) ALH from TROPOMI and AEH from GEMS over ocean and (c) over land (Black box and error bar is mean and standard deviation in 20% interval of each TROPOMI ALH) over the period from March 28 to 30, 2021.

Figure 9 shows intercomparison results for aerosol plume height among GEMS,

458 CALIOP, and TROPOMI during the case study of dust transport in East Asia from
459 March 28 to 30, 2021. For the direct comparison shown in Figure 9a, the difference in
460 AEH between GEMS and CALIOP was -0.13±1.32 km. Nanda *et al.* (2020) reported
461 that the difference in ALH between TROPOMI and CALIOP was 0.53 km for 4 cases of
462 thick Saharan dust plumes. Large AEH uncertainty occurred mostly over the inland area
463 of China. Because AEH from GEMS uses only the O_2-O_2 absorption band, the accuracy
464 of AEH is sensitive to uncertainty in surface reflectance and AOD. From Park et al.
465 (2016), total error budget of AEH is 0.74-1.28 km, and the total error budget considered
466 the uncertainty of AOD, SSA, aerosol particle size, and surface albedo in the aerosol
467 retrieval process. The total error budget amount from the previous study is similar
468 value of standard deviation of AEH difference between GEMS and CALIOP.
469 Figures 9b and 9c illustrate the comparison results between GEMS AEH and
470 TROPOMI ALH, for the period of March 28-30, 2021, over land and ocean surface,
471 respectively. The difference between GEMS AEH and TROPOMI ALH was 0.72 ± 0.84
472 km and 1.71 ± 0.77 km over ocean and land in this case, respectively. In addition, 82.4%
473 and 37.3% of all pixels had differences of less than 1.5 km over ocean and land,
474 respectively. However, the ALH from TROPOMI is generally lower than the AEH from
475 GEMS because of the discrepancy in definitions. Based on the assumption of aerosol
476 vertical distribution for AEH retrieval, the difference between AEH and center height of
477 aerosol extinction profile is around 0.5 km. To consider the inconsistency of definition
478 between ALH and AEH, the difference between two retrieval results decreased to 0.5
479 km bias. After consideration of definition inconsistency, the proportion of pixels within
480 the expected error ranges of 1.5 km are enhanced to 92.1% and 65.0% over ocean and
481 land, respectively.

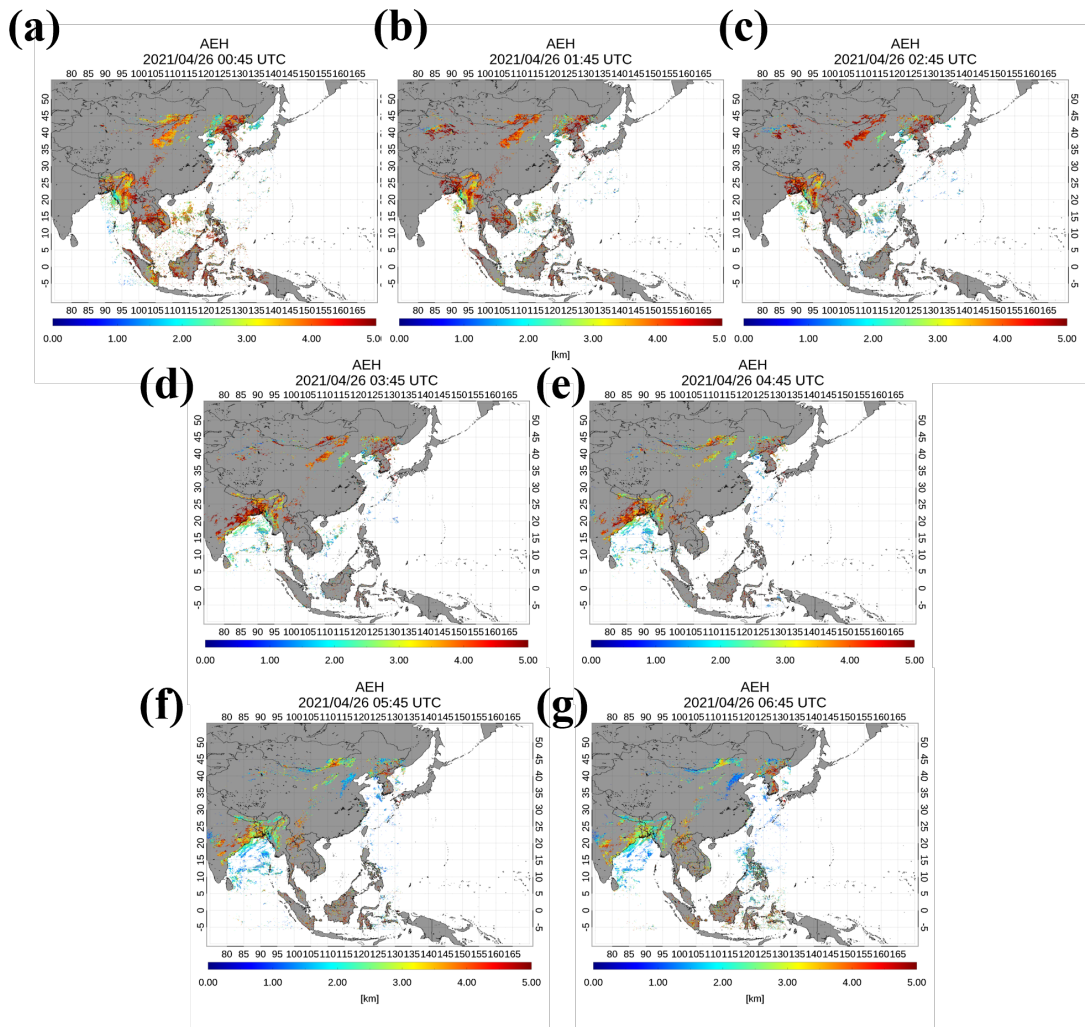

Figure 10. Case study results for AEH based on GEMS observations on April 26, 2021 [(a) 00:45 UTC, (b) 01:45 UTC, (c) 02:45 UTC, (d) 03:45 UTC, (e) 04:45 UTC, (f) 05:45 UTC, and (g) 06:45 UTC].

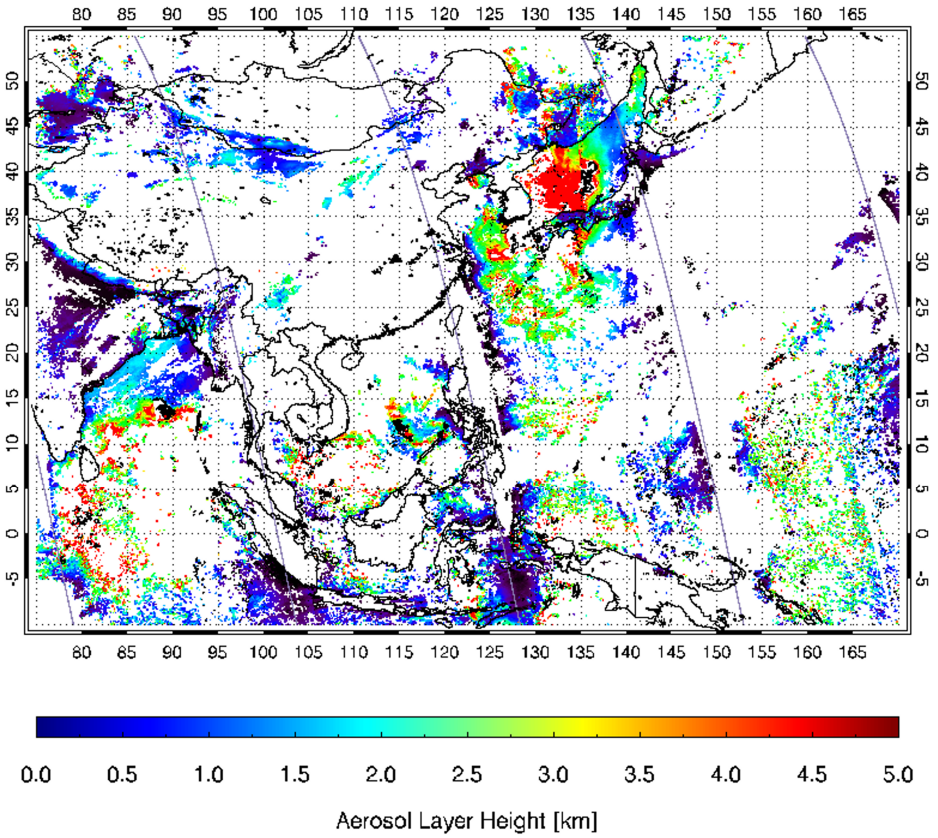

Figure 11. ALH retrieved from TROPOMI and orbit path of CALIOP on April 26, 2021 (Unit: km).

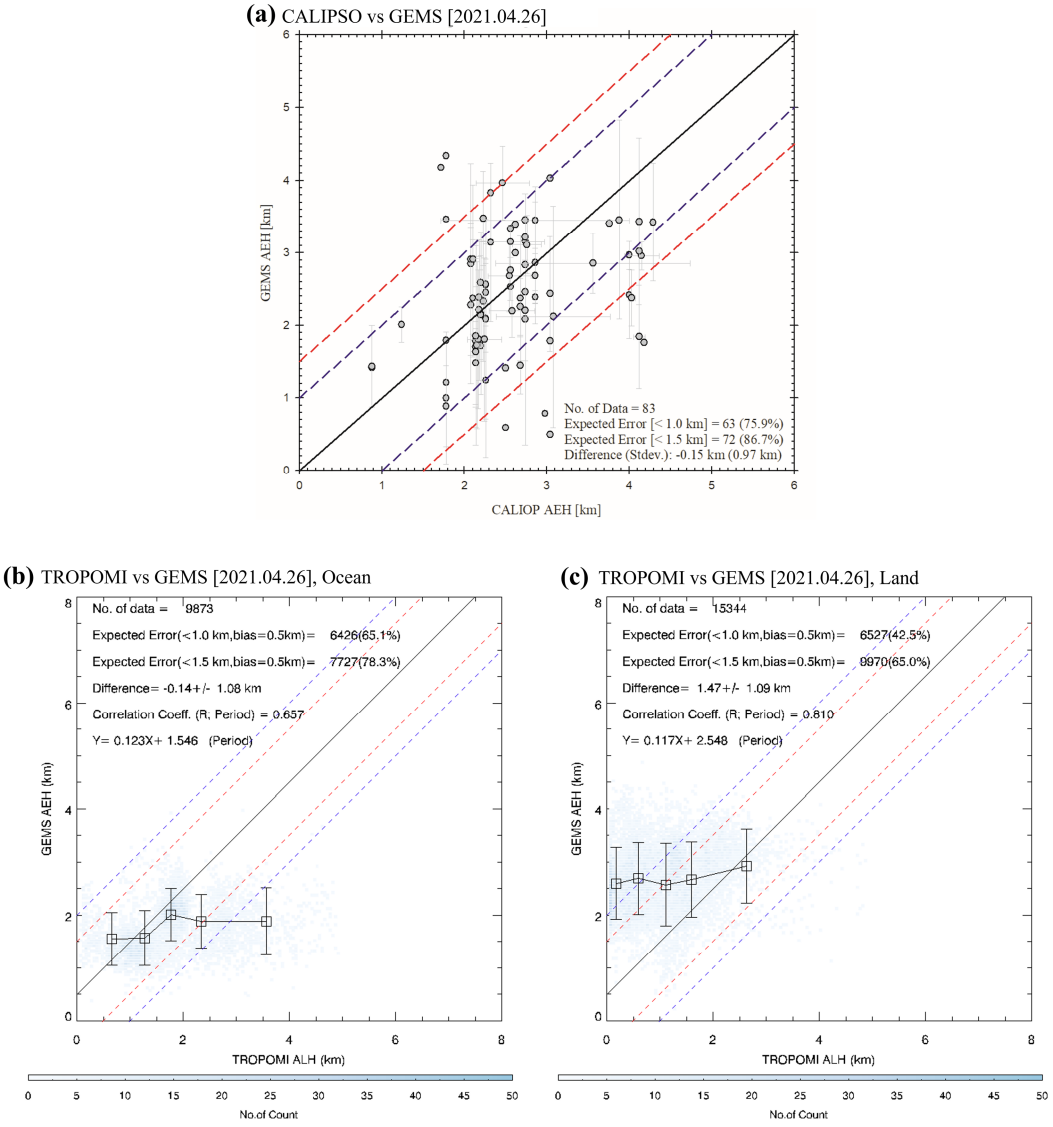

Figure 12. Intercomparison of (a) AEH between CALIOP and GEMS, and (b) ALH from TROPOMI and AEH from GEMS over ocean and (c) over land (black dot and error bar is mean and standard deviation in 20% interval of each TROPOMI ALH) on April 26, 2021.

An additional intercomparison case of April 26, 2021, is shown in Figures 10 (GEMS) and 11 (TROPOMI). During the transport of the dust plume from inland China to the coastal area, AEH changed from 4.0 km at 02:00 UTC to 2.0 km at 06:00 UTC.

By contrast, ALH from TROPOMI only observed the 1.5-2.5 km layer height over East Asia around 04:00 UTC. Although the AEH from GEMS had spatio-temporal uncertainty, this case demonstrates the advantage of AEH retrieval from GEMS for continuous monitoring of changes in plume height during dust transport, in particular. As shown in Figure 12, AEH from GEMS showed differences in height of -0.15 ± 0.97 km (compared to CALIOP). In addition, the differences in height of -0.14 ± 1.06 and 1.47 ± 1.09 km over ocean and land as compared to TROPOMI ALH.

From two different case results, proportion values within 1.0 km (or 1.5 km) height difference between TROPOMI and GEMS have strong dependence of surface types. The proportion over land (over ocean) was lower (higher) than the corresponding result from the comparison of GEMS and CALIOP. The TROPOMI ALH from version 2 exhibits a strong surface type dependence as compared to the ground lidar data (Michailidis et al., 2023). However, the relationship between TROPOMI ALH and GEMS AEH in 20% interval of each TROPOMI ALH have high correlation coefficients. In the case of March 28-30, the correlation coefficients between TROPOMI and GEMS are 0.663 and 0.993 over ocean and land, respectively. In the case of April 26, the correlation coefficients are 0.657 and 0.810 over ocean and land, respectively.

5. Long-term validation

For long-term validation, we used the AEH retrieval results from January to June, 2021. The CALIOP and TROPOMI satellites passed over the study area around 13:30 local time, which is around 04:30 UTC for East Asia and around 06:30 UTC for India. Most temporal colocation pixels aligned with observation times of 04:00-06:00 UTC, respectively. To check the dependence of several retrieval variables, the UVAI, AOD,

SSA, and dominant aerosol type in each pixel (TYPE) were obtained from the L2AERAOD. Although the GEMS algorithm retrieved AEH in the range of 0-10 km, the sensitivity of O_2-O_2 SCD to the optical path length was weak in cases of high AEH because the vertical distribution of O_2-O_2 SCD is related to the square of the air molecule densities. To ensure sufficient quality of retrieved data, therefore, the AEHs from GEMS and CALIOP, and the ALH from TROPOMI were used only in pixels where the AEH from GEMS were lower than 5 km.

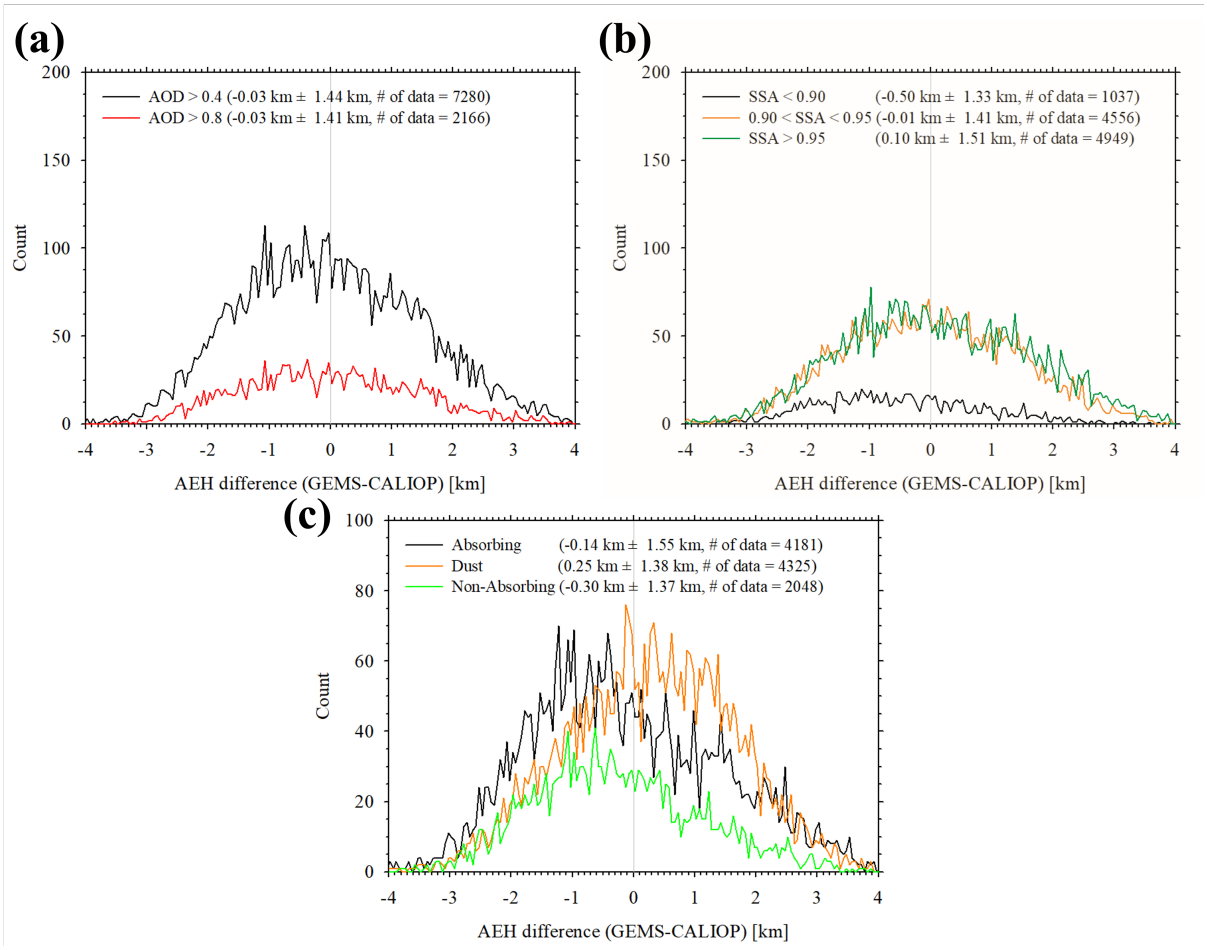

Figure 13. Histogram of AEH difference between CALIOP and GEMS with respect to (a) AOD, (b) SSA, and (c) TYPE from GEMS over the period from January 1 to June 30, 2021.

Figure 13 shows histograms of difference in AEH between GEMS and CALIOP according to AOD_{443}, SSA_{443}, and TYPE from GEMS. From Figure 13a, the dependence on AOD threshold was insignificant; the average estimated AEH difference was -0.03 km, but the variation in AEH difference was around 1.4 km based on the standard deviation for AOD_{443} > 0.4. Because of uncertainty in GEMS aerosol operational products, AEH from GEMS exhibits large variability. Although L2AERAOD from GEMS retrieved the AOD, SSA, and aerosol types, the retrieved results from L2AERAOD include significant uncertainty. Go et al. (2020) reported that the root-mean square error (RMSE) of AOD between MODIS and OMI UV aerosol algorithm is 0.276-0.341.

In addition, fitting error perturbs the fitting signals and tends to result in the underestimation of SCD. Although the fitting error of O_2-O_2 SCD from GEMS radiance was minimized, the fitting error has still remained around 6%, as indicated in Table 2. The discrepancy in fitting condition between the simulated and observed radiance biased the SCD estimation, which in turn led to bias and variation in the AEH retrieval. Combined with the high sensitivity of AEH errors to aerosol optical properties, uncertainty arising from L2AERAOD causes AEH variability.

The variation in AEH difference between observation platforms is shown in Figure 13b as a histogram according to SSA threshold. Across the entire SSA threshold range, the standard deviation of the AEH difference was 1.33-1.51 km. In particular, this standard deviation decreased slightly with decreasing SSA. The aerosol height parameter is more sensitive to absorbing-dominant aerosols than scattering-dominant aerosols (e.g., Park *et al.*, 2016; Nanda *et al.*, 2020). For this reason, the variability of AEH is smaller in absorbing-dominant aerosols than scattering-dominant aerosols, if the

557 uncertainty of other aerosol parameters (AOD, SSA, and TYPE) is the same conditions.

558 Figure 13c shows the dependence of AEH difference on TYPE. The TYPE product
559 included dependence on the aerosol size and optical absorptivity. For this reason, the
560 AEH difference graphs for the “Dust” and “Absorbing” types differ, despite both types
561 being absorbing-dominant aerosols. The AEH difference for the “Absorbing” type
562 showed a negative bias with a large standard deviation, whereas a positive bias with a
563 small standard deviation was obtained for the “Dust” type. The AEH difference for the
564 “Non-Absorbing” aerosol type showed the largest negative bias in this comparison.
565 These results suggest that the aerosol size distribution of fine particles affects the
566 negative bias of AEH. Combined with the AEH difference bias illustrated in Figure 8b,
567 these findings indicate that the bias in AEH difference for “Absorbing” aerosols is
568 weakened by their absorbing-dominant property.

569 Figure 14 shows means and standard deviations for AEH difference between
570 CALIOP and GEMS according to AOD and AI values from GEMS. For AOD, the mean
571 AEH difference ranged from -0.13 to 0.03 km with a standard deviation of
572 approximately 1.45 km. Similar to Figure 13a, the variation in AEH difference with
573 AOD change was insignificant. For the AI, the lowest AEH difference was -0.19 km,
574 obtained for the AI range of 1.5-2.0. The largest AEH difference was 0.24 km for the AI
575 range of 4.0-4.5. Although the AEH difference varied slightly, no consistent tendency in
576 AEH variation with AI was observed. Overall, the standard deviation of AEH difference
577 ranged from 1.49 km ($0.0 < AI < 0.5$) to 1.18 km ($4.5 < AI < 5.0$), and a consistent
578 tendency of decreasing variance in AEH difference was found with increasing AI.

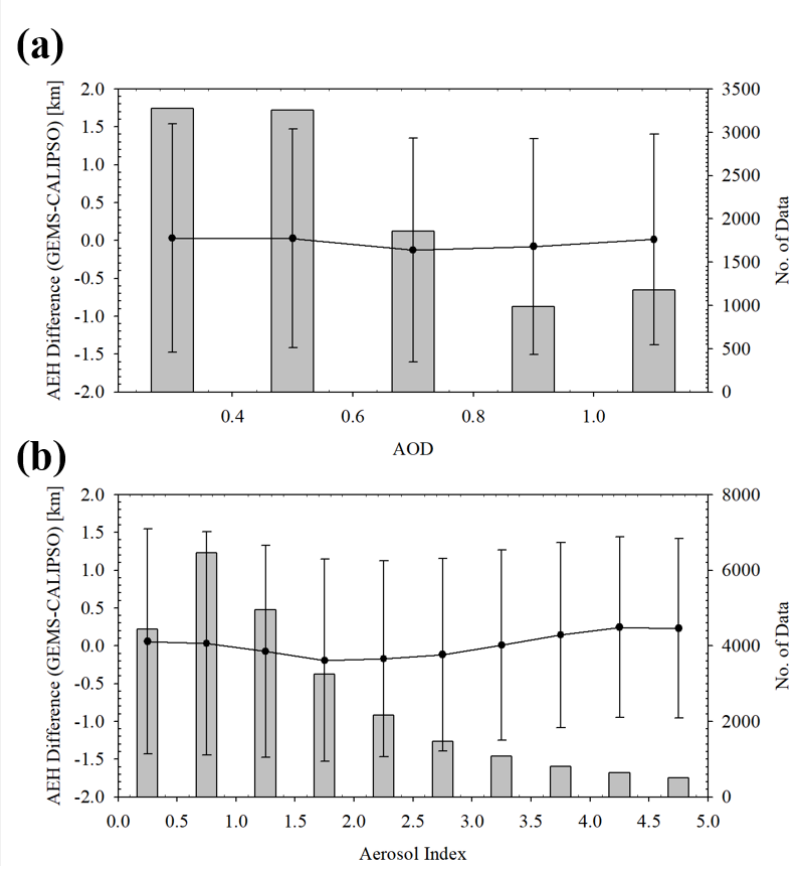

579

580 **Figure 14.** AEH difference between CALIOP and GEMS with respect to ranges of (a)
581 AOD and (b) AI obtained from GEMS from January 1 to June 30, 2021 (Black dots and
582 error bars denote the mean and standard deviation of AEH difference, while the gray-
583 box indicates the number of data).

584

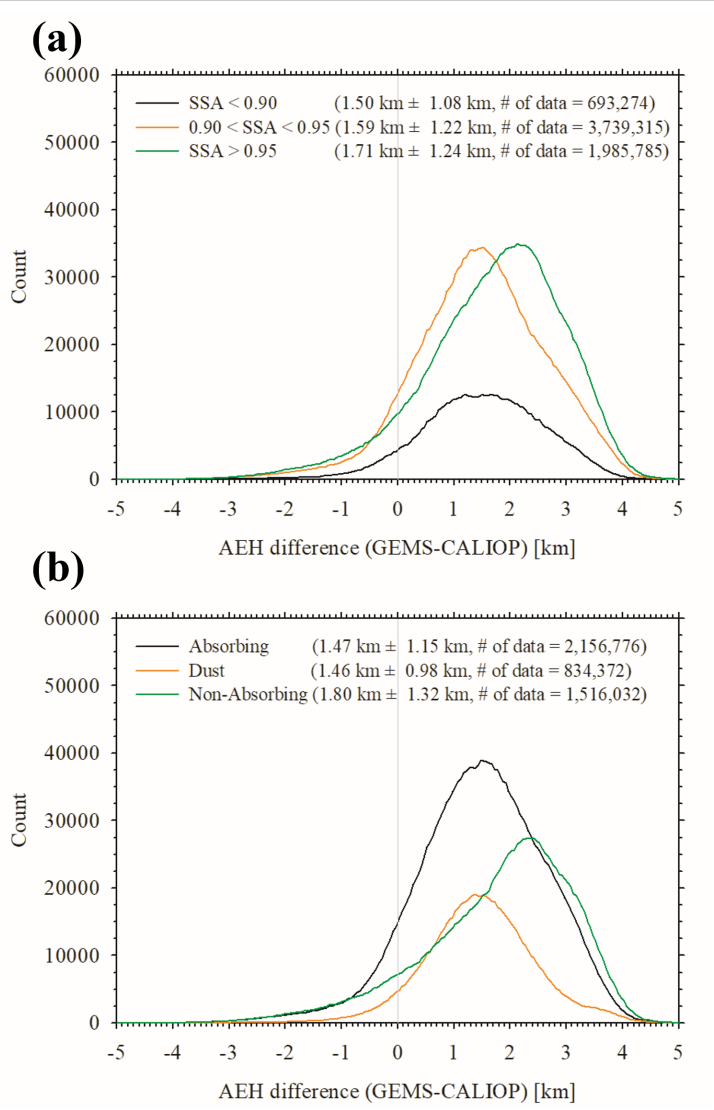

585

586 **Figure 15.** Histograms of differences between TROPOMI ALH and GEMS AEH
587 with respect to (a) SSA, and (b) TYPE from GEMS in the period from January 1 to June
588 30, 2021.

589

590 Figure 15 shows histograms of differences between GEMS AEH and TROPOMI
591 ALH according to the SSA_{443} and TYPE obtained from GEMS. The difference between
592 GEMS AEH and TROPOMI ALH depends on both SSA and TYPE. The mean
593 difference value between GEMS AEH and TROPOMI ALH decreased as the aerosol

absorptivity increased. This difference was 1.50 ± 1.08, 1.59 ± 1.22, and 1.71 ± 1.24 km for pixels of SSA_{443} < 0.90, 0.90 < SSA_{443} < 0.95, and SSA_{443} > 0.95, respectively. Comparing these results to Figure 13b, we find that the standard deviation of the comparison with TROPOMI was approximately 75% of the corresponding value for CALIOP. It is because both TROPOMI and GEMS are passive sensors that use similar retrieval methods for oxygen absorption bands. Nanda *et al.* (2020) showed that the operational algorithm of TROPOMI operational algorithm can provide ALH pixel retrievals only for scenes dominated by absorbing aerosol particles. In addition, Griffin *et al.* (2020) reported that the pixels with low positive UVAI values (weak absorbing cases) are identified with low QA values (QA ≤ 0.5) in the offline product of ALH. Although the TROPOMI ALH algorithm updated for the expansion of retrieval range, the contrast of O_2-O_2 SCD to the aerosol layer height change is fundamentally weak sensitivity in scattering dominant aerosols (e.g., Park et al., 2016). For this reason, the bias and standard deviation of height difference between GEMS and ALH is generally larger in high SSA.

In addition, the difference between GEMS AEH and TROPOMI ALH depends on TYPE, as shown in Figure 15b. The difference was 1.47 ± 1.15, 1.46 ± 0.98, and 1.80 ± 1.32 km for "Absorbing", "Dust", and "Non-Absorbing" type aerosols, respectively. Similar to Figure 13c, the TYPE dependence of aerosol height information was influenced by both absorptivity and size information. "Dust" type of aerosol is mainly transported in the free troposphere with gaussian-like vertical distribution, and the associated plume thickness is highly variable. However, "Absorbing" aerosols mainly originate from anthropogenic emissions in East Asia and mostly distributed near the surface with homogeneous concentration (e.g., Gao *et al.*, 2014; Wang *et al.*, 2012;

Peng *et al.*, 2016). Transport patterns and vertical distribution shape depending on aerosol types, can affect the accuracy of aerosol height retrieval results.

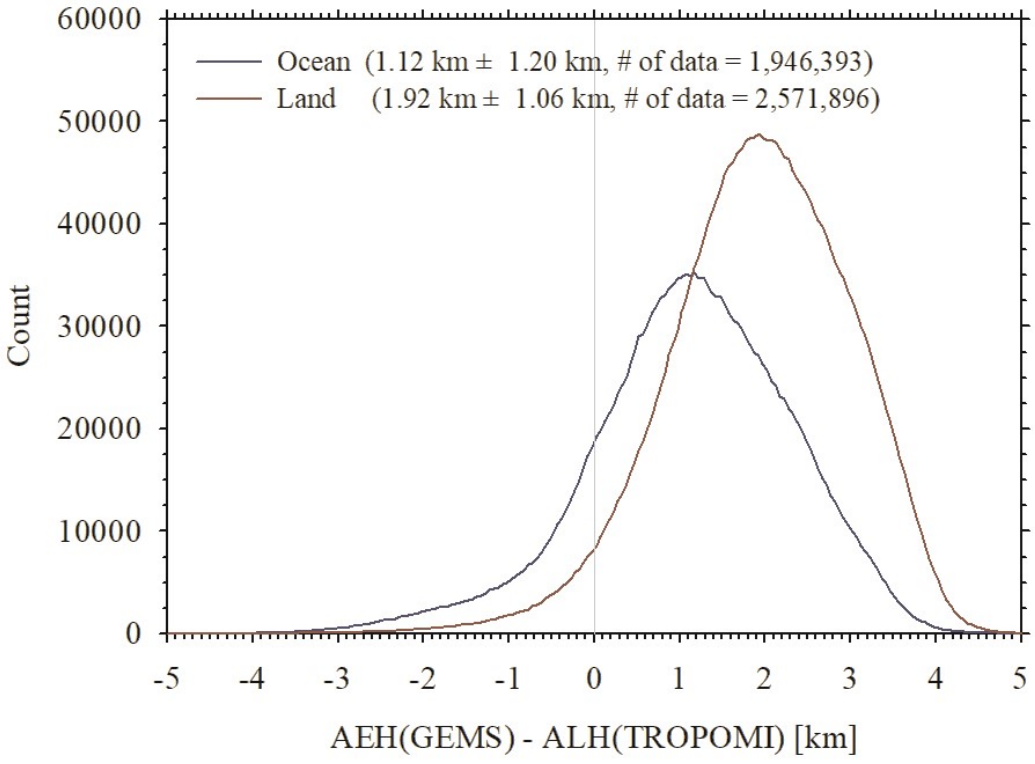

Figure 16. Histogram of the difference between TROPOMI ALH and GEMS AEH over land and ocean pixels, respectively, from January 1 to June 30, 2021.

The non-Lambertian effect on the land surface impacted surface albedo uncertainty during AEH retrieval, and this effect led to bias and variance in AEH. In this study, the minimum Lambertian equivalent reflectance was used as the reference reflectance value. However, surface reflectivity has geometric dependence due to non-Lambertian effects, which leads to a bias of 0.01-0.02 for surface reflectance over the land surface (e.g., Qin *et al.*, 2019). To identify the sensitivity of surface property, a histogram was constructed of difference between GEMS AEH and TROPOMI ALH after classification into land

and ocean surface types, as shown in Figure 16. From the statistical results, the mean differences were estimated to be 1.12 ± 1.20 and 1.92 ± 1.06 km for ocean and land pixels, respectively. The bias has significant difference between two different surface types. Michailidis et al. (2023) explained that the experimental retrieval range of ALH from TROPOMI is 0.27-6.5 km and 0.06-2.15 km over ocean and land, respectively. Constrained retrieval range over land by the TROPOMI influences the negative bias of aerosol height retrieval and increases the mean difference of aerosol height between GEMS and TROPOMI. In addition, the non-Lambertian effect for surface reflectance is also affecting the increasing discrepancy of aerosol height information.

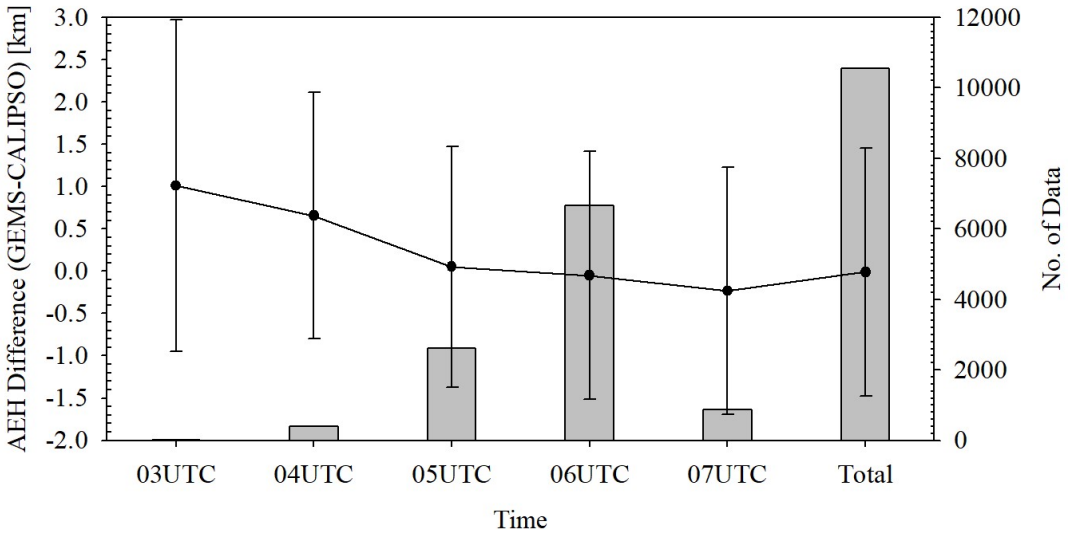

Figure 17. Diurnal dependence of AEH difference between CALIOP and GEMS from January 1 to June 30, 2021 (Black dots and error bars denote the mean and standard deviation of AEH difference, while the gray-box indicates the number of data).

The results of hourly statistical analyses are presented in Figure 17. Because they use a consistent definition of AEH, we show only a comparison of GEMS and CALIOP. The

diurnal variation in AEH difference ranged from -0.23 ± 1.45 km (07:00 UTC, Number of Data = 867) to 1.01 ± 1.96 km (03:00 UTC, Number of Data = 23). However, the number of pixels observed at 03:00 UTC was insufficient for the identification of diurnal variation of retrieval uncertainty. The AEH difference of 0.66 ± 1.45 km was the next highest value obtained at 04:00 UTC (Number of Data = 395). The inhomogeneous number of data is mainly due to the lack of spatial homogeneity among retrieval pixels. Over India, very high AOD values were consistently observed during the comparison period. Otherwise, the AEH was only retrieved under conditions of severe anthropogenic emissions over East Asia. In addition, the diurnal variation in AEH difference was caused by spatial characteristics of AEH difference. From 03:00 to 05:00 UTC, CALIOP mainly passed over East Asia, which has numerous sources of aerosol emissions, including biomass burning, dust, and industrial activity. In addition, GEMS observed only the eastern part of India, which is dominated by anthropogenic aerosols. The spatial distribution of the dominant aerosol types may impact the diurnal variation in AEH difference.

6. Summary & Conclusions

Based on the possibility of retrieving AEH from environmental satellite sensors, an AEH retrieval algorithm for GEMS was developed that solely uses the O_2-O_2 absorption band with considering of aerosol and surface properties. Because the sensitivity of AEH retrieval is strongly affected by optical depth and properties of aerosols, as well as surface reflectivity, the AEH retrieval algorithm for GEMS uses the GEMS operational product, L2AERAOD. With the newly developed retrieval algorithm, GEMS can be used to monitor aerosol vertical information with high temporal and spatial resolution.

For dust plumes over East Asia, AEH retrieval results from GEMS indicated appropriated aerosol vertical information. After spatial and temporal colocation, the AEH from GEMS aligned well with the AEH information obtained from CALIOP. The differences in AEH between GEMS and CALIOP for dust plume cases were -0.13 ± 1.32 and -0.15 ± 0.97 km, with 49.9-75.9% and 73.2-86.7% of all pixels showing differences less than 1.0 and 1.5 km, respectively. Large AEH uncertainty was found mostly over inland China due to uncertainty in surface reflectance and AOD over the land surface. In addition, AEH from GEMS was overestimated compared to the TROPOMI ALH results. The overestimation is partially caused by different definitions of ALH from TROPOMI and AEH from GEMS.

In long-term intercomparison with CALIOP, the average AEH difference was estimated to be -0.03 km, with a standard deviation of 1.4 km under the scenario of AOD > 0.4. The large variation in AEH difference between GEMS and CALIOP was caused by uncertainty in the input parameters estimated from L2AERAOD. In the long-term intercomparison against TROPOMI, this difference was dependent on both SSA and TYPE. The difference was 1.50 ± 1.08 km, 1.59 ± 1.22 km, and 1.71 ± 1.24 km for pixels with SSA < 0.90, 0.90 < SSA < 0.95, and SSA > 0.95, respectively. In addition, differences of 1.47 ± 1.15 km, 1.46 ± 0.98 km, and 1.80 ± 1.32 km were obtained for the “Absorbing”, “Dust”, and the “Non-Absorbing” types of aerosols, respectively. The AEH difference also has a diurnal dependence, which ranged from -0.23 ± 1.45 km to 1.01 ± 1.96 km, due to the spatial characteristics of dominant aerosol types.

The case studies and results of the long-term validation show that AEH retrieved from GEMS can provide information on aerosol vertical distribution, with applications in diverse research fields. The AEH results with the long-term statistical accuracy make

it possible to use the application study for AMF calculation of GEMS trace gas retrieval. In addition, AEH considerably affects the surface particulate matter (PM) concentration obtained from satellite-based AOD because PM estimation is significantly affected by the mixing layer height of aerosols. For this reason, the AEH can provide the effective mixing layer height of aerosols for anthropogenic aerosols and also provide the vertical patterns for long-range transport of aerosols.

Although several fields of study may apply the AEH retrieval results, retrieval uncertainty in AEH remains due to the uncertainty of retrieved AOD and SSA. In addition, the uncertainty in surface reflectance and the discrepancy in O_2-O_2 SCD values between the simulation results and observations can be affected to the potential error sources of AEH from GEMS. To minimize the AEH retrieval uncertainty, further analysis related to the optimized input parameters of AOD, SSA, and aerosol type information is essential. For this reason, the quantitative analysis of AEH uncertainty due to aerosol and surface property is important for the improvement of AEH retrieval algorithm. In addition, aerosol optical property retrieval by the visible channel will be needed for further study to improve the aerosol type determination. Although the aerosol indices of UV and visible provide the aerosol type information, developing the aerosol type classification algorithm is necessary to make synergy with AEH retrieval. AEH provides representative layer height information as only one variable because of its sole reliance on O_2-O_2 SCD for direct estimation of aerosol height information. This method is limited to the consideration of aerosol vertical structures (i.e., Gaussian or exponential vertical distribution structures). To increase the information contents, it would be valuable to combine other oxygen absorption bands from other satellite instruments together with extinction information of aerosols.

Data Availability

The TROPOMI ALH product is available from http://doi.org/10.5270/S5P-7g4iapn, and the CALIOP aerosol extinction profile product is available from https://doi.org/10.5067/CALIOP/CALIPSO/CAL_LID_L2_05kmAPro-Prov-V3-41. The GEMS AEH and AERAOD products are available from the Environmental Satellite Center in National Institute of Environmental Research (NIER) of the Republic of Korea.

Acknowledgements

This work was supported by the National Institute of Environment Research of the Republic of Korea under Grant NIER-2023-04-02-050.

References

Accarreta, J. R., de Haan, J. F., and Stammes, P.: Cloud pressure retrieval using the O2-O2 absorption band at 477 nm, J. Geophys. Res., 109, D05204, doi:10.1029/2003JD003915, 2004

Ahn, C., Torres, O., and Jethva, H.: Assessment of OMI near-UV aerosol optical depth over land, J. Geophys. Res., 119, 2457-2473, 2014.

Bogumil, K., Orphal, J., Burrows, J. P., and Flaud, J. M.: Vibrational progressions in the visible and near-ultraviolet absorption spectrum of ozone, Chem. Phys. Lett., 349, 241-248, 2001.

Buchard, V., de Silva, A. M., Colarco, P. R., Darmenov, A., Randles, C. A., Govindaraju, R., Torres, O., Campbell, J., and Spurr, R.: Using the OMI aerosol index and absorption aerosol optical depth to evaluate the NASA MERRA Aerosol reanalysis, Atmos. Chem. Phys., 15, 5743-5760, 2015.

Chen, X., Wang, J., Xu, X., Zhou, M., Zhang, H., Garcia, L. C., Colarco, P. R., Janz, S. J., Yorks, J., McGill, M., Reid, J. S., de Graaf, M., and Kondragunta, S.: First retrieval of absorbing aerosol height over dark target using TROPOMI oxygen B band: Algorithm development and application for surface particulate matter estimates, Remote Sens. Env., 265, 112674, 2021.

Chen, X., Xu, X., Wang, J., and Diner, D. J.: Can Multi-angular polarimetric measurements in the oxygen-A and B bands improve the retrieval of aerosol vertical distribution?, J. Quant., Spectro. Rad. Trans., 270, 107679, 2021.

Chimot, J., Veefkind, J. P., Vlemmix, T., de Haan, J. F., Amiridis, V., Proestakis, E., Marinou, E., and Levelt, P. F.: An exploratory study on the aerosol height retrieval from OMI measurements of the 477 nm O2-O2 spectral band using a neural network approach, Atmos. Meas. Tech., 10, 783-809, 2017.

Choi, H., Liu, X., Abad, G. G., Seo, J., Lee, K. -M., and Kim, J.: A fast retrieval of cloud parameters using a Triplet of wavelengths of oxygen dimer band around 477 nm, Remote Sens., 13, 152, doi: 10.3390/rs13010152, 2021.

Choi, W., Lee, H., Kim, J., Ryu, J. -Y., Park, S. S., Park, J., and Kang, H.: Effects of spatiotemporal O4 column densities and temperature-dependent O4 absorption cross-section on an aerosol effective height retrieval algorithm using the O4 air

762 mass factor from the ozone monitoring instrument, Remote Sens. Env., 229, 223-
763 233, 2019.
764 Choi, W., Lee, H., and Kim, J.: First TROPOMI retrieval of aerosol effective height
765 using O4 absorption band at 477 nm and aerosol classification, IEEE Trans.
766 Geosci., Remote Sens., 59, 9873-9886, 2021.
767 de Graaf, M., Stammes, P., Torres, O., and Koelemeijer, R. B. A.: Absorbing aerosol
768 index: Sensitivity analysis, application to GOME and comparison with TOMS, J.
769 Geophys. Res., 110, D01201, doi:10.1029/2004JD005178, 2005.
770 de Graaf, M., de Haan, J. F., and Sanders, A. F. J.: TROPOMI ATBD of the Aerosol
771 Layer Height, issue 2.4.0, 2022-04-08,
772 https://sentinel.esa.int/documents/247904/2476257/Sentinel-5P-TROPOMI-
773 ATBD-Aerosol-Height, 75pp, Royal Netherlands Meteorological Institute,
774 Netherland, last access: 15 June, 2024.
775 Ding, S., Wang, J., and Xu, X.: Polarimetric remote sensing in oxygen A and B bands:
776 Sensitivity study and information content analysis for vertical profile of aerosols,
777 Atmos. Meas. Tech, 9, 2077-2092, 2016.
778 Dubuisson, P., Frouin, R., Dessaily, D., Duforet, L., Leon, J. –F., Voss, K., and Antoine,
779 D.: Estimating the altitude of aerosol plumes over the ocean from reflectance ratio
780 measurements in the O2 A-band, Remote Sens. Environ., 113, 1899-1911,
781 doi:10.1016/j.rse.2009.04.018, 2009.
782 European Space Agency*, TROPOMI Level 2 Aerosol Layer Height products. Version*
783 *02.* https://doi.org/10.5270/S5P-7g4iapn, 2021.
784 Gao, Y., Zhao, C., Liu, X., Zhang, M., and Leung, L. R.: WRF-Chem simulations of
785 aerosols and anthropogenic aerosol radiative forcing in East Asia, Atmos. Environ.,
786 92, 250-266, 2014.
787 Geddes, A., and Boesch, H.: Tropospheric aerosol profile information from high-
788 resolution oxygen A-band measurements from space, Atmos. Meas. Tech., 8, 859-
789 874, 2015.
790 Go, S., Kim, J., Park, S. S., Kim, M., Lim, H., Kim, J. -Y., Lee, D. -W., and Im, J.:
791 Synergistic use of hyperspectral UV-visible OMI and broadband meteorological
792 imager MODIS data for a merged aerosol product, Remote Sens., 12, 3987,
793 doi:10.3390/rs12233987, 2020.

Griffin, D., Sioris, C., Chen, J., Dickson, N., Kovachik, A., de Graaf, M., Nanda, S., Veefkind, P., Dammers, E., McLinden, C. A., Makar, P., and Akingunola, A.: The 2018 fire season in North America as seen by TROPOMI: aerosol layer height intercomparisons and evaluation of model-derived plume heights, Atmos. Meas. Tech., 13, 1427-1445, 2020.

Herman, J. R., Bhartia, P. K., Torres, O., Hsu, C., Seftor, C., and Celarier, E.: Global distribution of UV-absorbing aerosols from Nimbus-7/TOMS data, J. Geophys. Res., 102(D14), 16911-16922, 1997.

Hong, H., Lee, H., Kim, J., Jeong, U., Ryu, J., and Lee, D. S.: Investigation of simultaneous effects of aerosol properties and aerosol peak height on the air mass factors for space-borne NO2 retrievals, Remote Sens., 9, 208, doi:10.3390/rs9030208, 2017.

Joiner, J., and Bhartia, P. K.: The determination of cloud pressures from rotational Raman scattering in satellite backscatter ultraviolet measurements, J. Geophys. Res., 100, 23019-23026, 1995.

Joiner, J., and Vasilkov, A. P.: First results from the OMI rotational Raman scattering cloud pressure algorithm, IEEE Trans. Geosci. Remote Sens., 44, 1272-1282, 2006.

Kim, M., Kim, J., Torres, O., Ahn, C., Kim, W., Jeong, U., Go, S., Liu, X., Moon, K. J., and Kim D. -R.: Optimal estimation-based algorithm to retrieve aerosol optical properties for GEMS measurements over Asia, 10, 162, doi:10.3390/rs10020162, 2018.

Kim, J., Jeong, U., Ahn, M. -H., Kim, J. H., Park, R. J., Lee, H., Song, C. H., Choi, Y. -S., Lee, K. -H., Yoo, J. -M., Jeong, M. -J., Park, S. K., Lee, K. -M., Song, C. -K., Kim, S. -W., Kim, Y. J., Kim, S. -W., Kim, M., Go, S., Liu, X., Chance, K., Chan Miller, C., Al-Saadi, J., Veihelmann, B., Bhartia, P. K., Torres, O., González Abad, G., Haffner, D. P., Ko, D. H., Lee, S. H., Woo, J. -H., Chong, H., Park, S. S., Nicks, D., Choi, W. J., Moon, K. -J., Cho, A., Yoon, J., Kim, S. -K., Hong, H., Lee, K., Lee, H., Lee, S., Choi, M., Veefkind, P., Levelt, P. F., Edwards, D. P., Kang, M., Eo, M., Bak, J., Baek, K., Kwon, H. -A., Yang, J., Park, J., Han, K. M., Kim, B. -R., Shin, H. -W., Choi, H., Lee, E., Chong, J., Cha, Y., Koo, J. -H., Irie, H., Hayashida, S., Kasai, Y., Kanaya, Y., Liu, C., Lin, J., Crawford, J. H., Carmichael, G. R., Newchurch, M. J., Lefer, B. L., Herman, J. R., Swap, R. J., Lau, A. K. H., Kurosu,

826 T. P., Jaross, G., Ahlers, B., Dobber, M., McElroy, C. T., and Choi, Y.: New era of
827 air quality from Space: Geostationary Environment Monitoring Spectrometer
828 (GEMS), Bul. Ame. Meteorol. Soc., 101(1), E1–E22, 2020.
829 Koffi, B., Schulz, M., Bréon, F.-M., Griesfeller, J., Winker, D., Balkanski, Y., Bauer, S.,
830 Berntsen, T., Chin, M., Collins, W. D., Dentener, F., Diehl, T., Easter, R., Ghan, S.,
831 Ginoux, P., Gong, S., Horowitz, L. W., Iversen, T., Kirkevåg, A., Koch, D., Krol,
832 M., Myhre, G., Stier, P., and Takemura, T.: Application of the CALIOP layer
833 product to evaluate the vertical distribution of aerosols estimated by global models:
834 AeroCom phase I results, J. Geophys. Res.-Atmos., 117,
835 D10201, https://doi.org/10.1029/2011jd016858, 2012.
836 Kokhanovsky, A. A., and Rozanov, V. V.: The determination of dust cloud altitudes from
837 a satellite using hyperspectral measurements in the gaseous absorption band, Int. J.
838 Rem. Sens., 31, Nos. 9-10, 2729-2744, 2010.
839 Kooreman, M. L., Stammes, P., Trees, V., Sneep, M., Tilstra, L. G., de Graaf, M.,
840 Zweers, D. C. S., Wang, P., Tuinder, O. N. E., and Veefkind, J. P.: Effects of cloud
841 on the UV absorbing aerosol index from TROPOMI, Atmos. Meas. Tech., 13,
842 6407-6426, 2020.
843 Lee, J., Kim, J., Song, C. H., Kim, S. B., Chun, Y., Sohn, B. J., and Holben, B. N.:
844 Characteristics of aerosol types from AERONET sunphotometer measurements.
845 Atmos. Env., 44, 3110-3117, 2010.
846 Lorente, A., Boersma, K. F., Yu, H., Doerner, S., Hilboll, A., Richter, A., Liu, M.,
847 Lamsal, L. N., Barkley, M., De Smedt, I., Van Roozendael, M., Wang, Y., Wagner,
848 T., Beirle, S., Liu, J. -T., Krotkov, N., Stammes, P., Wang, P., Eskes, H. J., and Krol,
849 M.: Structural uncertainty in air mass factor calculation for NO2 and HCHO
850 satellite retrieval, Atmos. Meas. Tech., 10, 759-782, 2017.
851 Michailidis, K., Koukouli, M. -E., Balis, D., Veefkind, J. P., de Graaf, M., Mona, L.,
852 Papagianopoulos, N., Pappalardo, G., Tsikoudi, I., Amiridis, V., Marinou, E.,
853 Gialitaki, A., Mamouri, R. -E., Nisantzi, A., Bortoli, D., Joao Costa, M., Salgueiro,
854 V., Papayannis, A., Mylonaki, M., Alados-Arboledas, L., Romano, S., Perrone, M.
855 R., and Baars, H.: Validation of the TROPOMI/S5P aerosol layer height using
856 EARLINET lidars, Atmos. Chem. Phys., 23, 1919-1940, 2023.

857 Nanda, S., de Graaf, M., Sneep, M., de Haan, J. F., Stammes, P., Sanders, A. F. J.,
858 Tuinder, O., Veefkind, J. P., and Levelt, P. F.: Error sources in the retrieval of
859 aerosol information over bright surfaces from satellite measurements in the oxygen
860 A band, Atmos. Meas. Tech., 11, 161–175, https://doi.org/10.5194/amt-11-161-
861 2018, 2018.
862 Nanda, S., de Graaf, M., Veefkind, J. P., Sneep, M., ter Linden, M., Sun, J., and Level, P.
863 F.: A first comparison of TROPOMI aerosol layer height (ALH) to CALIOP data,
864 Atmos. Meas. Tech., 13, 3043-3059, 2020.
865 National Institute of Environmental Research, Geostationary Environment Monitoring
866 Spectrometer (GEMS) Algorithm Theoretical Basis Document: Aerosol Retrieval
867 Algorithm, 42pp, Ministry of Environment, Korea, 2020.
868 Omar, A., Winker, D. M., Vaughan, M. A., Ju, Y., Trepte, C. R., Ferrare, R. A., Lee, K.-
869 P., Hostetler, C. A., Kittaka, C., Rogers, R. R., Kuehn, R. E., and Liu, Z.: The
870 CALIPSO automated aerosol classification and Lidar ratio selection algorithm, J.
871 Atmos. Ocean. Tech., 26, 10, 1994-2014, 2009.
872 Park, S. S., Kim, J., Lee, H., Torres, O., Lee, K. –M., and Lee, S. D.: Utilization of O4
873 slant column density to derive aerosol layer height from a space-borne UV-visible
874 hyperspectral sensor: Sensitivity and case study, Atmos. Chem. Phys., 16, 1987-
875 2006, doi:10.5194/acp-16-1987-2016, 2016.
876 Park, S. S., Takemura, T., and Kim, J.: Effect of temperature-dependent cross sections
877 on O4 slant column density estimation by a space-borne UV-visible hyperspectral
878 sensor, Atmos. Environ., 152, 98-110, 2017.
879 Park, S. S., Kim, S. -W., Song, C. -K., Park, J. -U., and Bae, K. -H.: Spatio-temporal
880 variability of aerosol optical depth, total ozone, and NO2 over East Asia: Strategy
881 for the validation to the GEMS Scientific Products, Remote Sens., 12, 2256, 2020.
882 Peng, J., Hu, M., Guo, S., Du, Z., Zheng, J., Shang, D., Zamora, M. L., Zeng, L., Shao,
883 M., Wu, Y. -S., Zheng, J., Wang, Y., Glen, C. R., Collins, D. R., Molina, M. J., and
884 Zhang R.: Markedly enhanced absorption and direct radiative forcing of black
885 carbon under polluted urban environments, Proc. Natl. Acad. Sci., 113, 4266-4271,
886 2016.

887 Penning de Vries, M. J. M., Beirle, S., and Wagner, T.: UV aerosol indices from
888 SCIAMACHY: Introducing the Scattering Index (SCI), Atmos. Chem. Phys., 9,
889 9555-9567, 2009.
890 Penning de Vries, M. J. M., Beirle, S., Hoermann, C., Kaiser, J. W., Stammes, P., Tilstra,
891 L. G., Tuinder, O. N. E., and Wagner, T.: A global aerosol classification algorithm
892 incorporating multiple satellite data sets of aerosol and trace gas abundances,
893 Atmos. Chem. Phys., 15, 10597-10618, 2015.
894 Prospero, J. M., Ginoux, P., Torres, O., Nicholson, S. E., and Gill T. E.: Environmental
895 characterization of global sources of atmospheric soil dust identified with the
896 Nimbus 7 total ozone mapping spectrometer (TOMS) absorbing aerosol product,
897 Rev. Geophys., 40, 1002, doi:10.1029/2000RG000095, 2002.
898 Qin, W., Fasnacht, Z., Haffner, D., Vasilkov, A., Joiner, J., Krotkov, N., Fisher, B., and
899 Spurr, R.: A geometry-dependent surface Lambertian-equivalent reflectivity
900 product for UV-vis retrievals – Part 1: Evaluation over land surfaces using
901 measurements from OMI at 466 nm, Atmos. Meas. Tech., 12, 3997-4017, 2019.
902 Rana, A., Jia, S., and Sarkar, S.: Black carbon aerosol in India: A comprehensive review
903 of current status and future prospects, Atmos. Res., 218, 207-230, 2019.
904 Sanders, A. F. J., de Haan, J. F., Sneep, M., Apituley, A., Stammes, P., Vieitez, M. O.,
905 Tilstra, L. G., Tuinder, O. N. E., Koning, C. E., and Veefkind, J. P.: Evaluation of
906 the operational Aerosol Layer Height retrieval algorithm for Sentinel-5 Precursor:
907 application to O2 A band observations from GOME-2A, Atmos. Meas. Tech., 8,
908 4947-4977, 2015.
909 Sanders, A. F. J. and de Haan, J. F.: TROPOMI ATBD of the Aerosol Layer Height
910 product, 2016.
911 Sanghavi, S., Martonchik, J. V., Landgraf, J., and Platt, U.: Retrieval of optical depth
912 and vertical distribution of particulate scatterers in the atmosphere using O2 A- and
913 B-band SCIAMACHY observations over Kanpur: A case study, Atmos. Meas.
914 Tech., 5, 1099-1119, 2012.
915 Spurr, R. "User's Guide VLIDORT Version 2.6, RT Solutions.", Cambridge, MA,
916 USA, 2013.

Spurr, R., and Christri, M.: On the generation of atmospheric property Jacobians from the (V)LIDORT linearized radiative transfer models, J. Quant. Spectrosc. Radiat. Transf., 142, 109-115, 2014.

Thalman, R., and Volkamer, R.: Temperature dependent absorption cross-sections of O2-O2 collision pairs between 340 and 630 nm and at atmospherically relevant pressure. Phys. Chem. Chem. Phys. 15, 15371e15381, 2013.

Torres, O., Bhartia, P. K., Herman, J. R., Ahmad, Z., and Gleason, J.: Derivation of aerosol properties from satellite measurements of backscattered ultraviolet radiation: Theoretical basis, J. Geophys. Res., 103(14), 17099-17110, 1998.

Torres, O., Decae, R., Veefkind, P., and de Leeuw, G.: OMI Aerosol Retrieval Algorithm, OMI Algorithm Theoretical Basis Document, Vol. III, Clouds, Aerosols and Surface UV Irradiance, NASA-KNMI ATBD-OMI-03, pp. 47-71, 2002.

Torres, O., Jethva, H., Ahn, C., Jaross, G., and Loyola, D. G.: TROPOMI aerosol products: evaluation and observations of synoptic-scale carbonaceous aerosol plumes during 2018-2020, Atmos. Meas. Tech., 13, 6789-6806, 2020.

Vandaele, A. C., Hermans, C., Simon, P. C., Carleer, M., Colin, R., Fally, S., Merienne, M. F., Jenouvrier, A., and Coquart, B.: Measurements of the NO2 absorption cross-section from 42000 cm-1 to 10000 cm-1 (238-1000 nm) at 220 K and 294 K, J. Quant. Spectrosc. Radiat. Transfer, 59, 3-5, 171-184, 1998.

Vasilkov, A., Joiner, J., Spurr, R., Bhartia, P. K., Levelt, P., and Stephens, G.: Evaluation of the OMI cloud pressures derived from rotational Raman scattering by comparisons with other satellite data and radiative transfer simulations, J. Geophys. Res., 113, D15S19, doi:10.1029/2007JD008689, 2008.

Vasilkov, A., Yang, E. -S., Marchenko, S., Qin, W., Lamsal, L., Joiner, J., Krotkov, N., Haffner, D., Bhartia, P. K., and Spurr, R.: A cloud algorithm based on the O2-O2 477 nm absorption band featuring an advanced spectral fitting method and the use of surface geometry-dependent Lambertian-equivalent reflectivity, Atmos. Meas. Tech., 11, 4093-4107, 2018.

Veefkind, J. P., Aben, I., McMullan, K., Foerster, H., de Vries, J., Otter, G., Claas, J., Eskes, H. J., de Haan, J. F., Kleipool, Q., van Weele, M., Hasekamp, O., Hoogeveen, R., Landgraf, J., Snel, R., Tol, P., Ingmann, P., Voors, R., Kruizinga, B., Vink, R., Visser, H., and Levelt, P. F.: TROPOMI on the ESA Sentinel-5 Precursor:

A GMES mission for global observations of the atmospheric composition for climate, air quality and ozone layer applications, Remote Sens. Env., 120, 70-83, 2012.

Veihelmann, B., Levelt, P. F., Stammes, P., and Veefkind, J. P.: Simulation study of the aerosol information content in OMI spectral reflectance measurements, Atmos. Chem. Phys., 7, 3115-3127, 2007.

Wang, R., Tao, S., Wang, W., Liu, J., Shen, H., Shen, G., Wang, B., Liu, X., Li, W., Huang, Y., Zhang, Y., Lu, Y., Chen, H., Chen, Y., Wang, C., Zhu, D., Wang, X., Li, B., Liu, W., and M, J.: Black carbon emissions in China from 1949 to 2050, Environ., Sci. Technol., 46, 7595-7603, 2012.

Winker, D. M., Vaughan, M. A., Omar, A. H., Hu, Y., Powell, K. A., Liu, Z., Hunt, W. H., and Young, S. A.: Overview of the CALIPSO mission and CALIOP data processing algorithms, J. Atmos. Oceanic Technol., 26, 2310-2323, 2009.

Xu, X., Wang, J., Yang, Y., Zeng, J., Torres, O., Yang, Y., Marshak, A., Reid, J., and Miller, S.: Passive remote sensing of altitude and optical depth of dust plumes using the oxygen A and B bands: First results from EPIC/DSCOVR at Lagrange-1 point, Geophys. Res. Lett., 44, 7544-7554, 2017.

Xu, X., Wang, J., Wang, Y., Zeng, J., Torres, O., Reid, J. S., Miller, S. D., Martins, J. V., and Remer, L. A.: Detecting layer height of smoke aerosols over vegetated land and water surfaces via oxygen absorption bands: hourly results from EPIC/DSCOVR in deep space, Atmos. Meas. Tech., 12, 3269-3288, 2019.

Zeng, Z. -C., Chen, S., Natraj, V., Le, T., Xu, F., Merrelli, A., Crisp, D., Sander, S. P., and Yung, Y. L.: Constraining the vertical distribution of coastal dust aerosol using OCO-2 O2 A-band measurements, Remote Sens. Env., 236, 111494, 2020.